# Symmetric and antisymmetric convection signals in the Madden-Julian oscillation. Part I: Basic modes in infrared brightness temperature

Wen-wen Tung*

*Department of Earth, Atmospheric, & Planetary Sciences, Purdue University, West Lafayette, USA*

Dimitrios Giannakis Andrew J. Majda

*Courant Institute of Mathematical Sciences, New York University, New York, USA*

* *Corresponding author address:* Wen-wen Tung, Department of Earth, Atmospheric, and Planetary Sciences, Purdue University, 550 Stadium Mall Drive, West Lafayette, IN 47907.
E-mail: wwtung@purdue.edu

## ABSTRACT

This work studies the significance of north-south asymmetry in convection associated with the 20–90-day Madden-Julian oscillation (MJO) propagating across the equatorial Indo-Pacific warm-pool region. Satellite infrared brightness temperature data in the tropical belt for the period 1983–2006 were decomposed into components symmetric and antisymmetric about the equator. Using a recent nonlinear objective method called nonlinear Laplacian spectral analysis, modes of variability were extracted representing symmetric and antisymmetric features of MJO convection signals, along with a plethora of other modes of tropical convective variability spanning diurnal to interannual time scales. The space-time reconstruction of these modes during the 1992–1993 TOGA COARE period is described in detail. In particular, the boreal winter MJO emerges as a single pair of modes in both symmetric and antisymmetric convection signals. Both signals originate in the Indian Ocean around 60° E. They coexist for all significant MJO events with a varying degree of relative importance which is affected by ENSO. The symmetric signals tend to be suppressed when crossing the Maritime Continent, while the antisymmetric signals are not as inhibited. Their differences in peak phase and propagation speed suggest fundamental differences in the underlying mechanisms. The multiscale interactions between the diurnal, MJO, and ENSO modes of convection were studied. It was found that the symmetric component of MJO convection is out of phase with the symmetric component of the diurnal cycle, while the antisymmetric component of MJO convection is in phase with the antisymmetric diurnal cycle. The former relationship breaks down during strong El Niño events, and both relationships break down during prolonged La Niñas.

# 1. Introduction

The Madden-Julian oscillation (MJO, e.g., Madden and Julian 1971, 1972) is an eastward-propagating, planetary-scale envelope of organized convective activity in the tropics. Characterized by gross features in the 20–90-day intraseasonal time range and zonal wavenumber 1–4, it dominates tropical variability in subseasonal time scales. Moreover, through tropical–extratropical interactions, it influences global weather and climate variability, fundamentally linking short-term weather forecasts and long-term climate projections (Waliser 2005). Observational studies of the seasonality of tropical intraseasonal variability have shown that the MJO signals migrate latitudinally with the seasonal cycle, peaking during boreal winter (e.g., Wang and Rui 1990; Wheeler and Hendon 2004; Zhang and Dong 2004; Masunaga 2007; Kikuchi et al. 2012). The strongest boreal winter MJO signals in deep convection and precipitation are asymmetric about the equator especially in the Western Pacific (e.g., Wheeler and Hendon 2004; Zhang and Dong 2004; Masunaga 2007), implying asymmetric heat sources associated with convection. Indeed, Zhang and Dong (2004) were not able to identify any single mean background variable to explain well the seasonality in both the Indian and Western Pacific Ocean. They also proposed that the seasonality of MJO serves as a higher-order validation against MJO simulations by GCM.

Atmospheric responses to heat sources symmetric and antisymmetric about the equator are of fundamental theoretical interest (Gill 1980). In particular, perhaps the simplest theoretical model of the MJO describes the phenomenon as the planetary-scale response of a moving heat source with prescribed propagation speed through the linear shallow-water equations for a first baroclinic mode (e.g., Matsuno 1966; Gill 1980; Chao 1987; Biello and Majda 2005; Wang and Liu 2011). Biello and Majda (2005), in their multiscale model for the planetary-scale circulation associated with MJO, have demonstrated the differences between equatorial and off-equatorial convective heat sources on the solutions.

The goal of this work is to study the significance of asymmetry in the MJO convection signals by contrasting predominantly symmetric versus predominantly antisymmetric events in the observational record, in which both signals tend to coexist by nature. In particular, we study the symmetric and antisymmetric components of satellite infrared brightness temperature ($T_B$) data over the tropical belt, extracted using an averaging method (e.g., Yanai and Murakami 1970; Wheeler and Kiladis 1999). The differences and similarities of the associated spatiotemporal patterns elucidate the interactions of the MJO with other important weather and climate processes, including the diurnal cycle and ENSO. Our methods and results are presented in a two-part series, in which the present paper addresses the extraction of spatiotemporal modes of variability (including the MJO) from the symmetric and antisymmetric components of $T_B$ data, as well as the apparent connection between some of the modes in space and across diurnal to interannual time scales. Part II (Tung et al. 2013) studies the kinematic and thermodynamic fields associated with predominantly equatorially symmetric and off-equatorial convection in phase composites constructed through the MJO modes recovered in Part I.

These objectives require meticulous analysis procedures, for convectively coupled tropical motions are highly nonlinear and multiscaled in time and space. Substantial advances in the understanding of tropical waves, MJO, and their linear theories have been guided for decades by linear methods including Fourier-based space-time filtering, regression, and empirical orthogonal functions (EOFs) (e.g., Hayashi 1979, 1982; Salby and Hendon 1994; Lau and Chan 1985; Kiladis et al. 2005, 2009; Waliser et al. 2009; Kikuchi and Wang 2010). However, further progress should benefit significantly from a paradigm shift of analysis methods. Specifically, theory has suggested that the MJO is a nonlinear oscillator (Majda and Stechmann 2009, 2011); in observations it was found that MJO may well be a stochastically-driven chaotic oscillator (Tung et al. 2011). Linear filtering of a nonlinear, chaotic system is known in principle to impede fundamental understanding of the system (Badii et al. 1988). In the long term, as data archives from observations, numerical simulations, and reanalysis continue to mount at record rates post the Year of Tropical Convection (May 2008 to April 2010) (e.g., Moncrieff et al. 2007, 2012), distilling these massive and heterogeneous datasets in order to gain scientific insight calls for minimally supervised analysis methods developed from first principles and efficient algorithms.

Here, we address the challenges associated with the multiscale nature and underlying nonlinear dynamics of tropical observational data through nonlinear Laplacian spectral analysis (NLSA, Giannakis and Majda 2012a,c, 2013; Giannakis et al. 2012); a recently-developed data analysis technique to extract spatiotemporal patterns from high-dimensional dynamical systems. NLSA builds a set of data-driven orthogonal basis functions on the discretely-sampled nonlinear data manifold. By lag-embedding the observed data via the method of delays, those basis functions differ crucially from classical Fourier modes in that they contain information about the time evolution (dynamics) of the system under study, and are also adapted to the geometrical structure of the data in phase space. Compared to extended empirical orthogonal functions (EEOFs, e.g., Lau and Chan 1985) and the equivalent singular spectrum analysis (SSA, e.g., Ghil et al. 2002), NLSA has high skill in capturing intermittent patterns, which carry little variance but may be of high dynamical significance (Crommelin and Majda 2004). Moreover, the method applies no preprocessing such as seasonal detrending or band-pass filtering, allowing one to simultaneously study processes spanning multiple timescales.

We find that the mode families extracted from the symmetric and antisymmetric $T_B$ components provide meaningful and complementary information about convective tropical variability on diurnal to interannual timescales. In particular, intraseasonal eastward-propagating modes representing the MJO emerge naturally in both symmetric and antisymmetric data, but these modes behave distinctly in their temporal and spatial evolution, with the antisymmetric modes exhibiting significantly higher intermittency in time and ability to propagate over the Maritime Continent. Moreover, the symmetric and antisymmetric MJO modes correlate in different ways with diurnal-scale processes over equatorial Africa, the Maritime Continent, and South America, with ENSO also playing a role. As a result, indices constructed through these modes probe distinct aspects of the MJO lifecycle and its interaction with other tropical convective processes. In Part II (Tung et al. 2013), horizontal and vertical wind, temperature, and humidity fields and their derived heat and moisture budget residuals associated with the significant equatorially symmetric and off-equatorial MJO convective events identified through the NLSA modes are reconstructed using reanalysis data.

The paper proceeds as follows. In section 2, we describe the data and methods used in this study. We present and discuss our results in sections 3–5, and conclude in section 6. Similarities and differences between the NLSA and SSA modes are discussed in an appendix.

# 2. Data and methods

### *a. CLAUS $T_B$: Proxy for tropical convective activity*

We analyze multi-satellite infrared brightness temperature ($T_B$) data from the Cloud Archive User Service (CLAUS) Version 4.7 (e.g., Hodges et al. 2000). Brightness temperature is a measure of the earth's infrared emission in terms of the temperature of a hypothesized blackbody emitting the same amount of radiation at the same wavelength ($\sim$ 10–11 $\mu$m in CLAUS). It is a highly correlated variable with the total terrestrial longwave emission. In the tropics, positive (negative) $T_B$ anomalies are associated with reduced (increased) cloudiness, hence suppressed (enhanced) deep convection. The global CLAUS $T_B(\Lambda, \Phi, t)$ data are on a 0.5° longitude ($\Lambda$) by 0.5° latitude ($\Phi$) fixed grid, with three-hour time ($t$) resolution from 00 UTC to 21 UTC, spanning July 1, 1983 to June 30, 2006. The values of $T_B$ range from 170 K to 340 K at approximately 0.67 K resolution.

The subset of the data in the global tropical belt between 15°S and 15°N was taken to create symmetric and antisymmetric averages about the equator, following the approach in

Yanai and Murakami (1970). The symmetric average is

$$\overline{T_B(\Lambda, t)} = \frac{1}{N} \sum_{\Phi=0^\circ}^{\Phi=15^\circ} \frac{T_B(\Lambda, -\Phi, t) + T_B(\Lambda, \Phi, t)}{2} , \tag{1}$$

where $N$ is the number of samples within the latitudinal ($\Phi$) range; negative values of $\Phi$ denote southern latitudes. Similarly, the antisymmetric average is

$$\overline{T_B(\Lambda, t)}_A = \frac{1}{N-1} \sum_{\Phi=0^\circ}^{\Phi=15^\circ} \frac{T_B(\Lambda, -\Phi, t) - T_B(\Lambda, \Phi, t)}{2} . \tag{2}$$

The resulting averages are longitude-time sequences sampled at $d = 720$ longitudinal gridpoints in $\Lambda$ and $s = 67{,}208$ temporal snapshots in $t$. Prior to spatial averaging, the missing data (less than 1%) were filled via linear interpolation in time. Figure 1 shows the portion of the data for 1992–1993; a period which includes the Intensive Observing Period (IOP) of the Tropical Ocean Global Atmosphere Coupled Ocean Atmosphere Response Experiment (TOGA COARE, November 1992–February 1993, Webster and Lukas 1992).

### *b. NLSA algorithms*

Nonlinear Laplacian spectral analysis (Giannakis and Majda 2012c,a, 2013) is a method for extracting spatiotemporal patterns from high-dimensional time series that blends ideas from the qualitative analysis of dynamical systems (Broomhead and King 1986; Sauer et al. 1991), singular spectrum analysis (SSA, Aubry et al. 1991; Ghil et al. 2002), and spectral graph theory for machine learning (Belkin and Niyogi 2003; Coifman and Lafon 2006). Unlike principal components analysis (PCA), EOFs, SSA, and related variance-maximizing algorithms, NLSA is based on the premise that dynamically-relevant low-rank decompositions of the data should be constructed via orthonormal basis functions which are intrinsic to the nonlinear data manifold sampled by the observations. The basis functions in question are Laplace-Beltrami (LB) eigenfunctions, computed via graph-theoretic algorithms (Belkin and Niyogi 2003; Coifman and Lafon 2006) after time-lagged embedding of the data to incorporate information about time-directed evolution.

Consider an $n \times s$ data matrix $\mathbf{X}$ consisting of $s$-samples of an $n$-dimensional variable. In section 3 ahead, each column of $\mathbf{X}$ will be either of the $\overline{T_B(\Lambda, t)}$ or $\overline{T_B(\Lambda, t)}_A$ fields from (1) and (2), respectively, embedded over an intraseasonal lag window $\Delta t$. NLSA produces a decomposition of the form

$$\mathbf{X} \approx \mathbf{U}_l \mathbf{\Sigma}_l \mathbf{V}_l^T \mathbf{\Phi}_l^T, \tag{3}$$

with $\mathbf{U}_l$ an $n \times l$ matrix with orthogonal columns, $\mathbf{\Sigma}_l$ an $l \times l$ diagonal matrix of singular values $\sigma_i$, $\mathbf{V}_l$ an $l \times l$ orthogonal matrix of expansion coefficients, and $\mathbf{\Phi}$ an $s \times l$ matrix of LB eigenfunction values. Each column $\mathbf{u}_i$ of $\mathbf{U}_l$ represents a spatiotemporal process of temporal extent $\Delta t$ analogous to an EEOF. The corresponding temporal pattern, analogous to a principal component (PC), is given by $\tilde{\mathbf{v}}_i = \mathbf{\Phi} \mathbf{v}_i$, where $\mathbf{v}_i$ is the $i$-th column of $\mathbf{V}_l$. The $\tilde{\mathbf{v}}_i$ are orthogonal with respect to a weighted inner product with weights $\boldsymbol{\mu}$ designed to capture rapid transitions and rare events (Giannakis and Majda 2012c).

The parameter $l$ corresponds to the number of LB eigenfunctions used in the NLSA decomposition, and in practice is significantly smaller than the number of samples. This type of data compression is especially beneficial in large-scale applications where the ambient space dimension $n$ and the sample number $s$ are both large (Giannakis and Majda 2013). Each triplet $\{\mathbf{u}_i, \sigma_i, \tilde{\mathbf{v}}_i\}$ yields a spatiotemporal process $\tilde{\mathbf{X}}_i = \sigma_i \mathbf{u}_i \mathbf{v}_i^T$ in lagged-embedding space, which can be projected down to physical space to produce reconstructions of the input signal (e.g., section 4).

The role of the transform matrix $\mathbf{\Phi}_l$ in (3) is to select geometrically-preferred temporal patterns on the nonlinear data manifold $M$. Such patterns are viewed in NLSA as good candidates to produce physically-meaningful EEOFs through weighted averages of the form $\mathbf{u}_i = \mathbf{X} \boldsymbol{\mu} \mathbf{v}_i$. In contrast, the classical SSA decomposition,

$$\mathbf{X} \approx \mathbf{U}_{SSA} \mathbf{\Sigma}_{SSA} \mathbf{V}_{SSA}^T \tag{4}$$

makes no such provision, and the temporal patterns $\mathbf{V}_{SSA}$ used for averaging can be arbitrary functions of time, without regards to the geometrical structure of $M$ other than global covariance. Note that the basis functions $\mathbf{\Phi}_l$ can encode multiple timescales of temporal variability despite being weakly oscillatory on the data manifold. This is because time variability in $\mathbf{\Phi}_l$ is an outcome of both their geometrical structure as functions on $M$, and the sampling of these functions along the trajectory on $M$ followed by the system under time evolution. For instance, the modes discussed in section 3 exhibit temporal variability spanning diurnal to interannual timescales, and yet are described in terms of a moderately small number of leading ("low-wavenumber") LB eigenfunctions.

The advantages of using (3) versus (4) have been demonstrated in a number of applications, including Galerkin reduction of dynamical systems where PCA is known to fail (Giannakis and Majda 2012c), and regression modeling in comprehensive climate models (Giannakis and Majda 2012a,b). Details of the NLSA methodology applied to the symmetrically averaged $T_B$, $\overline{T_B(\Lambda, t)}$, including parameter selection and computational considerations, are provided in Giannakis et al. (2012).

# 3. Modes of spatiotemporal variability revealed by NLSA

We have applied the NLSA algorithm described in section 2b using an intraseasonal embedding window spanning $\Delta t = 64$ days. This choice of embedding window was motivated from our objective to resolve propagating structures such as the MJO with intraseasonal (20–90 day) characteristic timescales. Unlike conventional approaches (e.g., Kikuchi et al. 2012; Maloney and Hartmann 1998; Wheeler and Hendon 2004), neither band-pass filtering nor seasonal partitioning was applied to the CLAUS dataset prior to analysis using NLSA.

The singular values $\sigma_i$ corresponding to the modes in (3) are displayed in Fig. 2. In Fig. 2a, several representative modes relevant to our analysis are identified in the symmetric $T_B$ data, namely an annual mode ($i = 1$), an interannual mode ($i = 2$), a pair of MJO modes

($i = 3, 4$), a pair of diurnal modes ($i = 5, 6$), and a "Maritime Continent" mode ($i = 11$). In addition, the symmetric spectrum contains a pair of modes featuring an intraseasonal peak together with interannual variability ($i = 7, 8$), as well as a pair of semiannual modes ($i = 9, 10$). In particular, the structure of the interannual–intraseasonal modes suggests that these modes may play a role in MJO–ENSO connection. We therefore refer to these modes as "Indo-Pacific intraseasonal–interannual". The modes in the spectrum beyond mode 11 generally describe intraseasonal and diurnal patterns which may also reveal meaningful aspects of tropical convective variability. However, due to the compression of information in the original two-dimensional (2D) fields occurring in the averaged data, we defer a detailed study of these modes to future analysis via NLSA of the full 2D CLAUS dataset.

Turning to the antisymmetric data, it takes at least four leading modes to account for the semiannual, annual, and interannual variability in the antisymmetrically averaged $T_B$ field. In Fig. 2b, in addition to an annual mode ($i = 1$) similar to that in the symmetric data, the subsequent three modes are likely associated with African, south Asian, and American monsoons ($i = 2$), intraseasonal, seasonal, and interannual variability over the eastern Pacific ITCZ ($i = 3$), as well as the intraseasonal to semiannual variability over Africa, Indian Ocean, and the South Pacific Convergence Zone (SPCZ) ($i = 4$). Additional modes of interest in Fig. 2b are two MJO modes ($i = 5, 7$) and two diurnal modes ($i = 6, 8$). Unlike their symmetric counterparts, the antisymmetric MJO and diurnal modes do not appear consecutively in the $\sigma_i$ spectrum. It is later found that the amplitude of these diurnal modes is strongly modulated by the MJO.

Representative spatiotemporal ($\mathbf{u}_i$) and temporal ($\mathbf{v}_i$) patterns associated with the modes described above are displayed in Figs. 3–5. For consistency with Fig. 1, the temporal patterns are shown for the duration of 1992–1993 in Figs. 3 and 4, along with their frequency spectra calculated from the entire $\sim$ 20-year-long time series. Below is a discussion of these patterns, which is followed in section 4 by further interpretation in the context of space-time reconstructions during the TOGA-COARE IOP.

*(i) Intraseasonal to interannual time scales*

The spatial patterns of the symmetric annual and interannual modes are nearly constant within the 64-day embedding window (Figs. 3a,b). Their corresponding temporal patterns reveal that these two modes explain the seasonal and longer-time variability of cloudiness in the tropical belt (Figs. 5a,b). Figure 3b features a dipole over the equatorial Pacific, suggesting that this mode is the primary ENSO mode. The semiannual pair, a member of which is shown in Figs. 3h and 5h, essentially captures the annual march of intensified deep convection in the ITCZ, SPCZ, Indo-Pacific warm pool, monsoons, and tropical storm tracks across the Southern and Northern Hemispheres. This pair of modes explains the apparent east-west migration and amplitude modulation of convection signals reflecting the north-south asymmetry in land mass and bathymetry within the tropical belt where the average is taken. The frequency spectrum also bears discernible power on the intraseasonal and interannual timescales.

The leading two modes of the antisymmetric data explain the annual cycle (Figs. 4a,b and 5j,k). The spatial patterns of antisymmetric annual cycle require two modes within the 64-day embedding window: one is in a nearly constant state indicating the convection centers presiding in one hemisphere (Fig. 4a); the other describes the inter-hemispheric crossing of convection centers, for which timing varies longitude-wise (Fig. 4b). The temporal patterns of these modes are in quadrature (Figs. 5j,k), and both exhibit semiannual spectral peaks. However, these peaks are not as pronounced as those in the next two modes (Figs. 5p,q), which are predominantly of semiannual character.

The spatial patterns of these two antisymmetric semiannual modes are divided between the Eastern and the Western Hemispheres and overlap over the Indian Ocean (Figs. 4c,d). In particular, the semiannual mode in Fig. 4c is centered in the Western Hemisphere, most notably over the Eastern Pacific. Its temporal pattern during 1992–1993 shows that it is more active in the boreal summer than in the boreal winter; its frequency spectrum shows significant variability on the interannual time scale (Fig. 5p). The spatial variability of the second semiannual mode is centered over the Indian Ocean, with a relatively weaker signal occurring over the Pacific. Its temporal pattern shows notable intraseasonal variability (Fig. 5q). The temporal patterns of the semiannual pair are roughly in quadrature during 1992–1993, with the amplification of $\mathbf{v}_4$ apparently leading that of $\mathbf{v}_3$ by about a month in the boreal spring to summertime (Figs. 5p,q).

*(ii) Intraseasonal eastward-propagating signals*

The symmetric MJO modes (MJO1 and MJO2; Figs. 3d,e and 5c,d), the antisymmetric MJO modes ($\mathrm{MJO1_A}$ and $\mathrm{MJO2_A}$; Figs. 4e,f and 5l,m), the symmetric Indo-Pacific intraseasonal–interannual modes (Figs. 3f,g and 5f,g), and the symmetric Maritime Continent mode (Figs. 3i and 5i) are eastward propagating modes with pronounced intraseasonal variability, characterized by broad peaks within the 20–90-day range in their frequency spectra. All of the symmetric modes are more or less suppressed around 110°E (Figs. 3d–g). The spatial patterns of MJO1 and MJO2 are in quadrature, indicating that together they represent the propagation of MJO convection (roughly of global wavenumber two) over the Indian Ocean–Western Pacific sector. The spatial patterns of $\mathrm{MJO1_A}$ and $\mathrm{MJO2_A}$ exhibit a similar behavior. Unlike the symmetric modes, whose maximum values tend to be confined over the oceans (Figs. 3d,e), the antisymmetric MJO modes have significant local extrema over land mass such as around 30°E, 120°E, and 75°W (Figs. 4e,f). Moreover, the global extrema of the symmetric modes are in the Indian Ocean around 90°E, while those of the antisymmetric modes extend further east into the Pacific such as 120°E and the date line. The temporal patterns of MJO1, MJO2, $\mathrm{MJO1_A}$, and $\mathrm{MJO2_A}$ show that these modes, especially the antisymmetric ones, are essentially boreal winter–spring modes (Figs. 5c,d and 5l,m).

The spatial patterns of the symmetric Indo-Pacific intraseasonal–interannual modes appear to be complementary to MJO1 and MJO2 and explain additional variability over the Indian Ocean and in the Western Pacific near the date line (Figs. 3f,g). The spatial patterns of these two modes are clearly in quadrature, with maximum amplitudes in the Indian

Ocean, suggesting a propagating pattern together. Unlike MJO2 and MJO2, however, the temporal patterns of these modes are active semiannually in boreal summer–fall as well as winter–spring and exhibit interannual variability (Figs. 5f,g).

The spatial pattern of the Maritime-Continent mode indicates that it has a smaller longitudinal range than the MJO modes. It does not propagate much beyond 150°E (3i). During 1992–1993, its temporal pattern appears to be active independently from MJO1 and MJO2 modes, although it could have been amplified with the presence of the latter two (Figs. 5c,d, and i). Note that the Indo-Pacific intraseasonal–interannual modes and the Maritime–Continent modes have a common intraseasonal spectral peak at $\sim$30 days, significantly shorter than that of the MJO modes.

*(iii) Diurnal cycle*

There are several modes in the NLSA spectrum for which the diurnal cycle is the most prominent timescale of variability. The spatial patterns of both symmetric diurnal modes, one of which is shown in (Fig. 3c), and antisymmetric diurnal modes (Figs. 3g,h) are most prominent over land, where the diurnal cycle of convection is most active. The major difference between the symmetric and the antisymmetric modes is seen in the Western Hemisphere over South America and part of Africa. For instance, unlike the symmetric modes, the antisymmetric diurnal cycle around 60°W is as strong as that over 30°E. Such contrast can be easily explained by the antisymmetric land mass over the Western Hemisphere in the analysis domain. The more subtle difference is over the Maritime Continent area, where the antisymmetric diurnal cycle has more substantial magnitude. The temporal patterns of the symmetric diurnal modes (Fig. 5e) are drastically different from those of the antisymmetric modes (Figs. 5n,o). The former appear to take place year-round, while the latter are strongly modulated by the seasonal cycle. Mode Diurnal1$_{\mathrm{A}}$ (Fig. 5n) is stronger in the boreal winter–spring and weaker in the boreal summer–fall. Mode Diurnal2$_{\mathrm{A}}$ (Fig. 5o) is evidently a boreal winter–spring mode.

# 4. Reconstruction of 1992–1993

We validate our mode reconstructions using the well-studied MJO events occurring in the TOGA-COARE IOP (hereafter, COARE IOP). The two complete MJOs observed during that period (e.g., Lin and Johnson 1996b,a; Tung et al. 1999; Yanai et al. 2000) can be seen in the longitude-time section of the symmetric CLAUS $T_B$ in Fig. 1a. Marked by two distinct envelopes of cold $T_B$ "supercloud clusters" (Nakazawa 1988), these systems propagated eastward from the Indian Ocean to the date line. The first event initiated near 75°E in late November, subsequently crossed the Maritime Continent around 100°–150°E, and disappeared near 170°W around January 10. The second event, being slightly faster than the first, started around January 5, and reached the central Pacific in early February. Concurrent signals in the antisymmetric $T_B$ can be seen for these two events (Fig. 1b). A weaker event took place in October 1992, prior to the start of the COARE IOP. Unlike the two strong cases, this event neither exhibited a significant symmetric component beyond the Maritime Continent (Fig. 1a), nor left a discernible trace in the antisymmetric $T_B$ (Fig. 1b).

The COARE IOP was coincident with the amplifying phase of an El Niño event. Therefore, the MJO events propagated further east beyond the date line, where during normal years the cold sea surface temperature is not conducive to deep convection (e.g., Chen and Yanai 2000; Kessler 2001). The influence of ENSO on MJO propagation is particularly evident in the January–May 1992 portion of Fig. 1, where ENSO was stronger than during the COARE IOP. MJO convection not only propagated further east beyond the date line during that period, but also exhibited significant off-equatorial (i.e., antisymmetric) characteristics. In all of the above cases, the eastward propagating speed of the MJO was $\sim$ 4–5 m s$^{-1}$. The convective systems around the Maritime Continent were especially complicated before, during, and after the passages of the MJO. In addition, two regions of apparently standing convection over equatorial Africa and America were observed (Figs. 1ab).

*(iv) Annual and interannual modes*

Figures 6 and 7 show the 1992–1993 space-time reconstruction of the modes identified with unique markers in Fig. 2. In terms of the annual modes, the amplitude of the first antisymmetric mode was about twice as strong as that of the symmetric mode, which was then stronger than the second antisymmetric mode (Figs. 6a and 7a,b). This is understandable since the first antisymmetric mode accentuates the preferred Hemisphere for deep convection, i.e., the Southern (Northern) Hemisphere when antisymmetric $T_B$ is negative (positive).

The symmetric annual mode (Fig. 6a) indicates that the regions around 70–90° E over the Indian Ocean and $\sim$ 90° W over the Eastern Pacific entered the season of overall suppressed convection, while the Amazon basin around 60° W received overall enhanced convective activity between 15°S and 15°N from late November to early December during the COARE IOP. In addition, the antisymmetric modes (Figs. 7a,b) show that centers of deep convection dictated by the seasonal mean state moved to the Southern Hemisphere in late November to early December, likely with Africa and South America being the earliest, followed by the Indo-Pacific warm pool, and Western Atlantic being the latest. The symmetric interannual mode in Fig. 6b exhibits periods of suppressed deep convection over the Western Pacific accompanied with enhanced deep convection over the Eastern Pacific. The latter are features associated with ENSO. The interannual mode was in an amplifying phase during the COARE IOP, and in a strong phase in January–May 1992. These features are consistent with the ENSO observations stated earlier.

*(v) MJO and other eastward propagating modes*

Figure 6c shows the symmetric MJO signal reconstruction based on MJO1 and MJO2 modes. This reconstruction captures the salient features of the propagating envelope of the MJO deep convection, including the initiation of enhanced deep convection (hence cold anomalies) over the Indian Ocean, the passage over the Maritime Continent, and the arrival and demise near the date line. The two reconstructed COARE IOP MJO events propagated at a speed of $\sim$4–5 m s$^{-1}$. It is noteworthy that upon initiation at around 60° E, MJO events traveled through the region of Indian Ocean where the seasonal mean state suppressed deep convection (Figs. 6a,c). As seen in Fig. 7c, the antisymmetric MJO signal reconstruction also captures the two MJO events during COARE IOP, although with a slightly slower speed and weaker signal during the November 1992 event. This is consistent with the seasonal mean state of deep convection centers being less antisymmetric over the warm pool region when the November event took place (Figs. 7a,b). Therefore, it is possible that the symmetric MJO signal is the only mode present at the onset of a chain of boreal winter MJO events as long as the mean state is symmetric. On the other hand, the antisymmetric MJO signal was most pronounced during the strong ENSO in January–May 1992 in Fig. 7c. That signal extends further east beyond the date line than its symmetric counterpart, and therefore likely captures the interaction between MJO and the SPCZ (Matthews et al. 1996; Matthews 2012).

Wang and Rui (1990) and Jones et al. (2004) studied the climatology of tropical intraseasonal convection anomalies. The eastward-propagating type of convection anomalies originating in the Indian Ocean were divided into subtypes. Following Jones et al. (2004), the three subtypes include one with signals confined in the Indian Ocean that never fully develop significant eastward propagation towards the western Pacific, one starting with eastward propagation but turning northward over the Indian or Western Pacific summer monsoon regions (aka. summer Intraseasonal oscillation, ISO), and the MJO. The symmetric Indo-Pacific intraseasonal–interannual modes (Figs. 6e,f) and the Maritime Continent modes (Figs. 6h) may be mixed manifestations of the former two subtypes owing to the compression of two-dimensional spatial data into one dimension. In addition, since the Indo-Pacific intraseasonal–interannual modes also describe anomalous convective activity near the date line, they could be related to an EOF mode found in Kessler (2001) representing the MJO–ENSO connection through propagation of MJO events farther east in the Central Pacific. Indeed, the stronger of the two modes (Fig. 6e) exhibits enhanced deep convection past the

180° date line corresponding well with the enhanced deep convection in the primary ENSO mode (Fig. 6b). The symmetric Maritime Continent mode (Fig. 6h), moreover, exhibits an eastward propagating disturbance with a speed of $\sim$ 7–8 m s$^{-1}$. It mainly comprises of two deep convective systems, each with a zonal scale of order 5000 km, centered around 90°E and 135°E, respectively. This mode may represent convective activity around the Maritime Continent, which exists on its own but is modulated by the passing of the MJO.

The different propagation speeds among the symmetric MJO signal, the antisymmetric MJO signal, and the Maritime-Continent mode suggest fundamentally different mechanisms in operation. The MJO and the Maritime-Continent modes are therefore examined with the frequency-wavenumber spectral analysis of their space-time reconstructions over 1984–2005. Figures 8a,b show the frequency-wavenumber spectra of the 1984–2005 symmetric and antisymmetric $T_B$ data, respectively. The spectral power in each panel has been normalized by its the maximum value. By convention (e.g., Hayashi 1982; Takayabu 1994; Wheeler and Kiladis 1999), the spectra are overlaid with dispersion curves calculated by assuming a static base state, with the marked equivalent depths for each equatorially trapped shallow water wave type (Matsuno 1966; Lindzen and Matsuno 1968). These raw spectra indicate that eastward-moving MJO is the most dominant subseasonal signal in both symmetric and antisymmetric $T_B$. Indeed, both reconstructed symmetric and antisymmetric MJO modes exhibit their strongest spectral peaks in the eastward-moving, wavenumber 1–3, and 30–90-day range (Figs. 9a,b). On the other hand, the antisymmetric MJO has relatively stronger westward-moving components, and spreads more into higher wavenumbers than the symmetric MJO. The symmetric Maritime Continent mode (Fig. 9c) has a higher frequency peak at around 30 days. According to the reference dispersion curves, this mode may have convection-coupled Kelvin and Rossby wave components. However, we refrain from further interpretation of this mode prior to 2D NLSA.

*(vi) Semiannual–interannual linkage*

In addition to the eastward-propagating intraseasonal modes in the previous discussion, the symmetric and antisymmetric semiannual modes (see Fig. 2) also display notable interannual variability (Figs. 5h,p). The reconstruction based on the two symmetric semiannual modes is consistent with the intensification of Indian Ocean ITCZ to the south of the equator, the onset of Australian summer monsoon, and intensification of the SPCZ in the later half of the COARE IOP (Fig. 6g). Note that these processes were suppressed by the amplification of ENSO (Fig. 6b). A more evident disruption of semiannual variations happened during the strong ENSO in early 1992, as seen in Fig. 6b with the eastward shift of deep convection anomalous centers into the Eastern Pacific.

The reconstructed antisymmetric semiannual modes are shown in Figs. 7e,f. Unlike its symmetric counterpart, the antisymmetric semiannual-interannual mode (Fig. 7e) was negligible during the COARE IOP, being a mostly boreal summer mode (Fig. 5p). This mode characterizes the enhanced convection over boreal monsoon regions such as the Northern Indian Ocean (cf. Fig. 7a) as well as the tropical Atlantic in late boreal spring to early summer. At the same time, it shows enhanced convection to the south of the equator between 180°–120° W associated with the peak phase of ENSO in the previous winter (cf. Fig. 6b). This pattern is consistent with previous observational and modeling studies of the teleconnection mechanism known as the "tropical atmospheric bridge" between ENSO-induced SST anomalies in the central equatorial Pacific to remote tropical oceans one to two seasons after the peak phase of ENSO in the previous winter (e.g., Klein et al. 1999; Lau et al. 2005).

The antisymmetric intraseasonal–semiannual mode has maximum variability over the Indian Ocean, which is likely associated with the monsoon and intraseasonal variability in this region (Fig. 7f), somewhat resembling the symmetric Indo-Pacific intraseasonal–interannual modes (Fig. 6e,f). The anomalous convection over the Indian Ocean, moreover, forms a propagating dipole with equatorial Africa. It might suggest that several weeks after maximum enhanced convection occurs in the southern Africa, enhanced convection over the northern Indian Ocean reaches its maximum strength. Such feature would have been missed in the symmetric averaging. During the COARE IOP, it appears that enhanced convection of this mode over the Indian Ocean was to the north of the equator at the initiation of the first MJO in November, but shifted to the south upon the initiation of the second MJO. Note that the amplitude of this mode is weaker but still comparable to the antisymmetric MJO modes (cf. Fig. 7c). In the boreal summer, this mode is likely associated with the Indian summer monsoon and ISO (e.g., Yasunari 1979; Lau and Chan 1986; Knutson and Weickmann 1987; Wang and Rui 1990; Jones et al. 2004). Lawrence and Webster (2001) studied the interannual variations of the ISO in the Indian summer monsoon and found that the ISO–Indian monsoon relationship is independent of the ENSO–Indian monsoon relationship, which is consistent with our finding of two separate modes to account for the ENSO–Indian monsoon (Fig. 7e) and the ISO–Indian monsoon (Fig. 7f) connection. One conjecture for the linkage between the boreal spring–summer patterns of these two modes during 1992–1993 is: deep convection was enhanced in the northern Indian Ocean after the onset of South Asian summer monsoon, which was then enhanced through teleconnection by the Central Pacific ENSO SST anomaly reaching maximum in the previous winter.

*(vii) Diurnal modes*

The symmetric diurnal modes are a twofold-degenerate pair (Fig. 2). Upon reconstruction, they reveal the standing diurnal convective events occurring mainly over tropical Africa and South America (Fig. 6d). The signals over the Maritime Continent are relatively weak. These diurnal cycles are moderately modulated by the passing of MJO, particularly over the South American continent, but generally exist year-round. On the other hand, the antisymmetric diurnal modes in Fig. 7d are obviously in phase with the MJO over Africa, the Maritime Continent, and South America.

# 5. Linkage from diurnal to interannual scales

Figure 10 shows 2D phase spaces spanned by pairs of temporal patterns during 1992–1993. The arc-like trajectories in Figs. 10a,b indicate strong periodicity in the phenomena described by the two symmetric (MJO1, MJO2) and antisymmetric ($\mathrm{MJO1_A}$, $\mathrm{MJO2_A}$) MJO modes. The convectively active periods of the two COARE IOP MJO events, identified visually from Fig. 1a, are recorded here with green crosses and red dots marking the first and second events, respectively. It is conventional to define the magnitude of an event at a given time as the distance between the origin and the point on the trajectory at that time (e.g., Shinoda et al. 1998; Matthews 2000; Wheeler and Hendon 2004), i.e.

$$r_\mathrm{S}(t) = [\mathrm{MJO1}^2(t) + \mathrm{MJO2}^2(t)]^{1/2}, \quad r_\mathrm{A}(t) = [\mathrm{MJO1}_\mathrm{A}^2(t) + \mathrm{MJO2}_\mathrm{A}^2(t)]^{1/2} \tag{5}$$

Under this criterion, the second event has obviously stronger magnitude than the first. Each phase space can be divided into eight sections indicating eight MJO phases, which are marked by Roman numerals in Figs. 10a,b. These phases, which are cyclic by definition, are calibrated so that Phase I encompasses the time interval during which convective signals of the COARE IOP MJOs initiate over the equatorial Indian Ocean. Spatial field reconstructions for each phase are discussed in detail in Part II.

Figures 10c,d display the two symmetric (Diurnal1, Diurnal2) and antisymmetric diurnal ($\mathrm{Diurnal1_A}$, $\mathrm{Diurnal2_A}$) modes, respectively. As expected by the diurnal periodicity of these modes and the 3 h sampling interval of the data, the phase-space coordinates lie along rays passing through the origin, and separated by 45° polar angles. Comparing against the respective MJO modes, an interesting pattern emerges: the relatively strong symmetric MJO component during COARE IOP coincides with suppression of the symmetric diurnal cycle. In contrast, the stronger antisymmetric MJO component is associated with enhanced antisymmetric diurnal cycle. Because the antisymmetric diurnal modes are slaved to the seasonal cycle (section 3), it is natural to ask whether the simultaneous amplification of the antisymmetric diurnal and MJO modes observed during COARE IOP implies more broadly a seasonal regularity of antisymmetric signals in MJO events. Any deviation from such regularity would manifest itself as a breach between simultaneously large values of $r_{\mathrm{A}}(t)$ and the corresponding magnitude associated with the antisymmetric diurnal modes. Indeed, breaches of this type occur frequently in the two decades of available $T_B$ data, and are correlated with the amplitude and sign of the ENSO mode, as we now discuss.

Figure 11 displays the same modes as in Fig. 10 during the strong El Niño event from 1997 to 1998. As the ENSO event is amplifying, both symmetric and antisymmetric MJO signals are strong. As the ENSO reaches full strength, the symmetric MJO signal collapses while the antisymmetric MJO signal is weakened but remains present. Now, a different pattern is observed: signals of symmetric and antisymmetric MJO signals are positively correlated with those of the symmetric and antisymmetric diurnal cycle, respectively. Previous studies have shown Figure 12 shows the temporal patterns of the ENSO and Maritime Continent modes, as well as the magnitudes of the symmetric and antisymmetric MJO and diurnal modes. Strong and persistent positive values of ENSO temporal pattern in Figs. 12a1 and 12b1 indicate El Niño events, such as years 1986–1987, 1991–1992, 1994-1995, 1997–1998, and 2002–2003. On the other hand, prolonged negative values such as those from 1988–1989 and 1999–2001 mark the La Niña events. Note that the the significant events in the magnitude time series for the MJO and diurnal modes are only those with large positive values.

Because of their regular seasonal variability, the magnitude of the antisymmetric diurnal modes in Figs. 12a3 and 12b3 is a useful indicator to distinguish between the winter–spring and summer–fall months. The latter are characterized by high and low antisymmetric diurnal amplitude, respectively (note that the magnitude of the symmetric diurnal modes has no such seasonal dependence). It is then evident that even though the MJO modes are mostly winter-spring modes in Fig. 12a2, they appear much more irregular in Fig. 12b2. Such disparities may be explained with the chain of pronounced ENSO events starting with strong El Niño followed by years of La Niña states from early 1997 to late 2001. Upon close examination, at the amplifying stage of the El Niño event in 1997, both symmetric and antisymmetric MJO components were enhanced. Similar situations may have also taken place in 1990 and 2002. However, after the El Niño reached its full strength in 1998, the symmetric MJO component diminished, and so did the symmetric diurnal mode. The antisymmetric MJO and diurnal modes remain unaffected. This simultaneous suppression of symmetric MJO and diurnal modes also occurred in the winter of the 1991–1992 El Niño. In that winter, the symmetric MJO magnitude remained near or below the one standard deviation threshold, and the symmetric diurnal magnitude was below its temporal mean. During La Niña years, most notably from 1999–2001, both symmetric and antisymmetric MJO modes are suppressed, while the diurnal modes are unaffected or even enhanced. The interplay between the ENSO, MJO, and diurnal modes is also evident in Fig. 6.

In summary, during neutral and weak ENSO years, the symmetric MJO and diurnal modes are out of phase, whereas the antisymmetric MJO and diurnal modes are in phase. During significant El Niño events, the former relationship breaks down in the sense that the symmetric MJO and diurnal modes are both suppressed, probably due to strongly skewed MJO and convective activity in space. During significant La Niña events, the correlation between MJO and diurnal modes diminishes. This might be explained by the westward shift of warm SST in the Pacific Ocean, limiting the eastward propagation of MJOs, and thus weakening the magnitude of the associated temporal patterns. These conjectures should be further examined with NLSA applied to timeseries of 2D $T_B$ fields.

Note that the relationships between the convectively active phase of MJO and the diurnal cycle of deep convection have been studied for the Western Pacific warm pool during January–March 1979 (Sui and Lau 1992) and the COARE IOP (e.g., Chen and Houze 1997; Sui et al. 1997; Johnson et al. 1999), as well as over tropical oceanic regions and the Maritime Continent during 1998–2005 (Tian et al. 2006). Sui and Lau (1992) suggested that convective diurnal cycle over the Maritime Continent diminished during periods of active MJO convection. Tian et al. (2006), on the other hand, found that diurnal cycle of tropical deep convection was enhanced (reduced) over both land and water during the convectively active (suppressed) phase of the MJO. However, those results are not readily applicable to interpret our findings. The diurnal cycle–MJO relationships presented here are easily altered by the state of ENSO, which was not explicitly addressed in these previous studies; and unlike in the previous studies of diurnal cycles over the ocean, the diurnal modes presented here mainly describe the symmetric and antisymmetric signals of convective variability over tropical landmass such as Africa and South America, and the antisymmetric signal over the Maritime Continent.

# 6. Conclusions and future work

In this work, we have studied the significance of north-south asymmetry in convection associated with the 20–90-day MJO propagating across the equatorial Indo-Pacific warm-pool region using high-resolution satellite infrared brightness temperature data ($T_B$). Using nonlinear Laplacian spectral analysis (NLSA, Giannakis and Majda 2012c, 2013; Giannakis et al. 2012), a nonlinear manifold generalization of PCA, we decomposed the symmetric and antisymmetric averages of $T_B$ over the 15°S–15°N equatorial belt into families of spatiotemporal modes for the period 1983–2006 sampled every 3 h. No preprocessing such as seasonal detrending or intraseasonal bandpass filtering was applied. As a result, the recovered modes provide a multiscale decomposition of the data into modes of variability ranging from diurnal, intraseasonal, semiannual, annual, and interannual. Most of these modes are likely results of multiscale interactions in Nature, therefore exhibiting multiscale spectral characteristics.

MJO modes, occurring with significant strength mostly in boreal winter to spring, were recovered in each of the symmetric and antisymmetric datasets. Both symmetric and antisymmetric signals of MJO convection originate in the Indian Ocean around 60° E. They coexist for all significant MJO events, although with varying combination event by event most notably affected by the state of ENSO (Fig. 12n). The symmetric signal of MJO convection tends to peak over the Indian Ocean before being suppressed upon reaching the Maritime Continent around 120° E. It then regains partial strength in the Western Pacific (Fig. 6c). On the other hand, the antisymmetric signal of MJO convection is not as inhibited by the Maritime Continent and reaches maximum strength in the western Pacific (Fig. 7c). It propagates with a slightly slower phase speed than the symmetric signal, but travels further east into the SPCZ. Moreover, the antisymmetric MJO signal has a stronger westward-propagating component than its symmetric counterpart. These differences in peak phase and propagation speed indicate fundamental differences to the mechanisms leading to the manifestation of these signals. This is also suggested by frequency-wavenumber spectra (Figs. 9a,b).

Through the associated temporal patterns (analogous to PCs) of these two MJO modes, we created symmetric and antisymmetric MJO indices which were employed in turn to identify MJO events in the observation period with strong symmetric or antisymmetric components in the signals of deep convection. Another important distinction between the predominantly symmetric and antisymmetric MJO events concerns their relation with ENSO and the diurnal cycle (Fig. 12). During neutral ENSO and weak ENSO years, the symmetric MJO component is out of phase with the leading symmetric diurnal mode, while the antisymmetric MJO is in phase with the corresponding antisymmetric diurnal mode. The former relationship breaks down during strong El Niño events. Both relationships might break down during strong La Niña events.

The space-time reconstruction of the MJO and other NLSA modes during 1992–1993 was studied in detailed (see section 4). Two MJO events were observed during the TOGA-COARE IOP (November 1992–February 1993). In the beginning of 1992, a strong positive ENSO event took place in the background of two more significant MJO events. The reconstructions of broadband interannual to interannual modes serve as the background states for these MJO events (Figs. 6,7). An intriguing Maritime Continent mode was found representing a $\sim$30-day system with mixed equatorial Rossby wave and Kelvin wave signals that takes place throughout the year near the Maritime Continent (Figs. 9c and 6c). In addition, two eastward-propagating intraseasonal modes were recovered, explaining variability of the MJO at its initiation time over the Indian Ocean and its demise near the date line (Figs. 6e,f). The latter is critical for the depiction of MJO propagation under the influence of ENSO. Lastly, the intraseasonal–semiannual modes with strong variability over the Indian Ocean may be associated with the ISO in the boreal summer, in addition to the initiation of MJO in the boreal winter (Figs. 6e,f and 7f), among which the antisymmetric mode exhibit a dipole of anomalous convection over equatorial Africa and the Indian Ocean (Fig. 6f).

These findings motivate the reconstruction of the kinematic and thermodynamics fields associated with the symmetric and antisymmetric MJO modes, which are presented in the Part II of this work (Tung et al. 2013). We plan to study the challenging question of intermittent MJO initiation and termination, as well as the physical mechanisms of the multiscale interactions between interannual, intraseasonal and diurnal modes in future work involving NLSA of 2D fields.

*Acknowledgments.*

We thank Robert Houze Jr., Richard Johnson, Brandon Kerns, George Kiladis, Mitchell Moncrieff, Toshi Shinoda, Augustin Vintzileos, Duane Waliser, and Chidong Zhang for stimulating discussions. We appreciate the invaluable comments and corrections by three anonymous reviewers. AJM, DG, and WWT are partially supported by ONR MURI 25-74200-F7112. AJM and DG also acknowledge support from ONR DRI grants N25-74200-F6607 and N00014-10-1-0554. WWT also received partial support from NSF CMMI-0826119 and CMMI-1031958. Major results were obtained using the CLAUS archive held at the British Atmospheric Data Centre, produced using ISCCP source data distributed by the NASA Langley Data Center. The computations were performed at NYU CIMS and Purdue RCAC.

# APPENDIX

## Comparison with SSA

For completeness, we have compared the NLSA spatiotemporal patterns with the corresponding patterns recovered through SSA using the same $\overline{T_B(\Lambda,t)}_A$ and $\overline{T_B(\Lambda,t)}$ datasets and $\Delta t = 64$ d embedding window, examples of which are shown in Figs. 13 and 14. The main commonalities and differences between the two approaches are as follows.

For the first few modes in the top of the spectrum, the spatial patterns $\mathbf{u}_i$ are qualitatively similar, but the corresponding temporal patterns $\mathbf{v}_i$ and spatiotemporal reconstructions from SSA exhibit significantly weaker amplitude modulation than in NLSA. This behavior is especially prominent in the antisymmetric MJO modes, which are displayed in Figs. 13c,d and 14a for the 1992–1993 reference period. There, instead of the sharp amplitude modulation favoring winter MJO activity in the NLSA reconstructions in Fig. 6, the SSA MJO patterns occur as more or less continuous wavetrains, with no clear distinction between summer and winter activity. Likewise, the antisymmetric diurnal modes from SSA (Figs. 13e,f and 14b) persist at a nearly constant amplitude throughout the year without regards to season and/or passing of an MJO. Similar statements can be made about the symmetric MJO and diurnal modes, although in this case the differences in amplitude modulation between the NLSA and SSA modes are not as significant.

As one might expect, the two methods differ qualitatively for the low-variance modes lying further down in the spectrum (for other examples, see Giannakis and Majda 2012a,c). In particular, we have found no evidence of a mode analogous to the Maritime Continent mode in the SSA spectrum. Instead, the SSA spectrum contains several wavetrain-like modes featuring simultaneous eastward- and westward-propagating structures with no obvious physical interpretation. Moreover, the NLSA spectrum of the symmetric data contains a second set of diurnal modes (not discussed in this paper), which are mainly active over the Amazon region during boreal summer. A second set of diurnal modes also arises in SSA, but these modes are active over both the Congo and Amazon regions (i.e., they are qualitatively similar to the leading set of symmetric diurnal modes), and exhibit weak amplitude modulation.

# REFERENCES


Aubry, N., R. Guyonnet, and R. Lima, 1991: Spatiotemporal analysis of complex signals: Theory and applications. *J. Stat. Phys.*, **64**, 683–739, doi:10.1007/bf01048312.

Badii, R., G. Broggi, B. Derighetti, M. Ravani, S. Ciliberto, A. Politi, and M. A. Rubio, 1988: Dimension increase in filtered chaotic signals. *Phys. Rev. Lett.*, **60**, 979–982, doi:10.1103/PhysRevLett.60.979.

Belkin, M. and P. Niyogi, 2003: Laplacian eigenmaps for dimensionality reduction and data representation. *Neural Comput.*, **15**, 1373–1396, doi:10.1162/089976603321780317.

Biello, J. A. and A. J. Majda, 2005: A new multiscale model for the Madden-Julian oscillation. *J. Atmos. Sci.*, **62 (6)**, 1694–1721.

Broomhead, D. S. and G. P. King, 1986: Extracting qualitative dynamics from experimental data. *Phys. D*, **20 (2–3)**, 217–236, doi:10.1016/0167-2789(86)90031-x.

Chao, W., 1987: On the origin of the tropical intraseasonal oscillation. *J. Atmos. Sci.*, **44 (15)**, 1940–1949.

Chen, B. and M. Yanai, 2000: Comparison of the Madden-Julian oscillation (MJO) during the TOGA COARE IOP with a 15-year climatology. *J. Geophys. Res.*, **105**, 2139–2149.

Chen, S. S. and R. A. Houze, 1997: Diurnal variation and life-cycle of deep convective systems over the tropical Pacific warm pool. *Quarterly Journal of the Royal Meteorological Society*, **123 (538)**, 357–388, doi:10.1256/smsqj.53805.

Coifman, R. R. and S. Lafon, 2006: Diffusion maps. *Appl. Comput. Harmon. Anal.*, **21**, 5–30, doi:10.1016/j.acha.2006.04.006.

Crommelin, D. T. and A. J. Majda, 2004: Strategies for model reduction: Comparing different optimal bases. *J. Atmos. Sci.*, **61**, 2206–2217, doi:10.1175/1520-0469(2004)061⟨2206:sfmrcd⟩2.0.cO;2.

Ghil, M. et al., 2002: Advanced spectral methods for climatic time series. *Rev. Geophys.*, **40**, 1003, doi:10.1029/2000rg000092.

Giannakis, D. and A. J. Majda, 2012a: Comparing low-frequency and intermittent variability in comprehensive climate models through nonlinear Laplacian spectral analysis. *Geophys. Res. Lett.*, **39**, L10 710, doi:10.1029/2012GL051575.

Giannakis, D. and A. J. Majda, 2012b: Limits of predictability in the North Pacific sector of a comprehensive climate model. *Geophys. Res. Lett.*, **39**, L24 602, doi:10.1029/2012GL054273.

Giannakis, D. and A. J. Majda, 2012c: Nonlinear Laplacian spectral analysis for time series with intermittency and low-frequency variability. *Proc. Natl. Acad. Sci.*, **109 (7)**, 2222–2227, doi:10.1073/pnas.1118984109.

Giannakis, D. and A. J. Majda, 2013: Nonlinear Laplacian spectral analysis: Capturing intermittent and low-frequency spatiotemporal patterns in high-dimensional data. *Stat. Anal. Data Min.*, **6 (3)**, 180–194, doi:http://dx.doi.org/10.1002/sam.11171.

Giannakis, D., W.-w. Tung, and A. J. Majda, 2012: Hierarchical structure of the Madden-Julian oscillation in infrared brightness temperature revealed through nonlinear Laplacian spectral analysis. *Conference on Intelligent Data Understanding (CIDU)*, 55–62, doi:10.1109/CIDU.2012.6382201.

Gill, A. E., 1980: Some simple solutions for heat-induced tropical circulation. *Quart. J. Roy. Meteor. Soc.*, **106 (449)**, 447–462, doi:10.1002/qj.49710644905.

Hayashi, Y., 1979: A generalized method of resolving transient disturbances into standing and traveling waves by space-time spectral analysis. *J. Atmos. Sci.*, **36**, 1017–1029.

Hayashi, Y., 1982: Space-Time Spectral Analysis and its Applications to Atmospheric Waves. *J. Meteor. Soc. Japan*, **27 (11)**, 156–171.

Hodges, K., D. Chappell, G. Robinson, and G. Yang, 2000: An improved algorithm for generating global window brightness temperatures from multiple satellite infra-red imagery. *J. Atmos. Oceanic Technol.*, **17**, 1296–1312.

Johnson, R. H., T. M. Rickenbach, S. A. Rutledge, P. E. Ciesielski, and W. H. Schubert, 1999: Trimodal Characteristics of Tropical Convection. *J. Climate*, **12 (8)**, 2397–2418, doi:10.1175/1520-0442(1999)012⟨2397:TCOTC⟩2.0.CO;2.

Jones, C., L. M. V. Carvalho, R. W. Higgins, D. E. Waliser, and J.-K. E. Schemm, 2004: Climatology of tropical intraseasonal convective anomalies: 1979-2002. *J. Climate*, **17**, 523–539.

Kessler, W. S., 2001: EOF Representations of the Madden Julian Oscillation and Its Connection with ENSO. *J. Climate*, **14**, 3055–3061.

Kikuchi, K. and B. Wang, 2010: Spatiotemporal wavelet Transform and the multiscale behavior of the Madden-Julian Oscillation. *J. Climate*, **23 (14)**, 3814–3834, doi:10.1175/2010JCLI2693.1.

Kikuchi, K., B. Wang, and Y. Kajikawa, 2012: Bimodal representation of the tropical intraseasonal oscillation. *Climate Dyn.*, **38**, 1989–2000, doi:10.1007/s00382-011-1159-1.

Kiladis, G. N., K. H. Straub, and P. T. Haertel, 2005: Zonal and Vertical Structure of the MaddenJulian Oscillation. *J. Atmos. Sci.*, **62 (8)**, 2790–2809, doi:10.1175/JAS3520.1.

Kiladis, G. N., M. C. Wheeler, P. T. Haertel, K. H. Straub, and P. E. Roundy, 2009: Convectively coupled equatorial waves. *Rev. Geophys.*, **47**, doi:10.1029/2008RG000266.

Klein, S. A., B. J. Soden, and N. C. Lau, 1999: Remote sea surface temperature variations during ENSO: Evidence for a tropical atmospheric bridge. *J. Climate*, **12**, 917–932.

Knutson, T. R. and K. M. Weickmann, 1987: 30-60 day atmospheric oscillations- Composite life cycles of convection and circulation anomalies. *Mon. Wea. Rev.*, **115**, 1407–1436.

Lau, K. and P. Chan, 1985: Aspects of the 40-50 day oscillation during the northern winter as inferred from outgoing longwave radiation. *Mon. Wea. Rev.*, **113**, 1889–1909.

Lau, K. M. and P. H. Chan, 1986: Aspects of the 4050 day oscillation during the northern summer as inferred from outgoing longwave radiation. *Mon. Wea. Rev.*, **114**, 1354–1367.

Lau, N.-C., A. Leetmaa, M. J. Nath, and H. L. Wang, 2005: Influences of ENSO-induced IndoWestern Pacific SST anomalies on extratropical atmospheric variability during the boreal summer. *J. Climate*, **18**, 2922–2942.

Lawrence, D. M. and P. J. Webster, 2001: Interannual Variations of the Intraseasonal Oscillation in the South Asian Summer Monsoon Region. *J. Climate*, **14**, 2910–2922.

Lin, X. and R. H. Johnson, 1996a: Heating, moistening, and rainfall over the western Pacific warm pool during TOGA COARE. *J. Atmos. Sci.*, **53 (22)**, 3367–3383.

Lin, X. and R. H. Johnson, 1996b: Kinematic and thermodynamic characteristics of the flow over the western Pacific warm pool during TOGA COARE. *J. Atmos. Sci.*, **53 (5)**, 695–715.

Lindzen, R. S. and T. Matsuno, 1968: On the nature of large scale wave disturbances in the equatorial lower stratophere. *J. Meteor. Soc. Japan*, **46 (3)**, 215–221.

Madden, R. A. and P. R. Julian, 1971: Detection of a 40–50 day oscillation in the zonal wind in the tropical pacific. *J. Atmos. Sci.*, **28 (5)**, 702–708, doi:10.1175/1520-0469(1971) 028⟨0702:DOADOI⟩2.0.CO;2.

Madden, R. A. and P. R. Julian, 1972: Description of global-scale circulation cells in the tropics with a 40–50 day period. *J. Atmos. Sci.*, **29 (6)**, 1109–1123, doi:10.1175/1520-0469(1972)029⟨1109:DOGSCC⟩2.0.CO;2.

Majda, A. J. and S. N. Stechmann, 2009: The skeleton of tropical intraseasonal oscillations. *Proc. Nat. Acad. Sci.*, **106 (21)**, 8417–8422.

Majda, A. J. and S. N. Stechmann, 2011: Nonlinear dynamics and regional variations in the MJO skeleton. *J. Atmos. Sci.*, **68**, 3053–3071.

Maloney, E. D. and D. L. Hartmann, 1998: Frictional moisture convergence in a composite life cycle of the Madden-Julian oscillation. *J. Climate*, **11**, 2387–2403.

Masunaga, H., 2007: Seasonality and regionality of the Madden-Julian oscillation, Kelvin wave, and equatorial Rossby wave. *J. Atmos. Sci.*, **64 (12)**, 4400–4416, doi:10.1175/2007JAS2179.1.

Matsuno, T., 1966: Quasi-geostrophic motions in the equatorial area. *J. Meteor. Soc. Japan*, **44**, 25–43.

Matthews, A. J., 2000: Propagation mechanisms for the Madden-Julian oscillation. *Quart. J. Roy. Meteor. Soc.*, **126**, 2637–2651.

Matthews, A. J., 2012: A multiscale framework for the origin and variability of the South Pacific Convergence Zone. *Quart. J. Roy. Meteor. Soc.*, **138 (666)**, 1165–1178, doi:10.1002/qj.1870.

Matthews, A. J., B. Hoskins, J. Slingo, and M. Blackburn, 1996: Development of convection along the SPCZ within a Madden-Julian oscillation. *Quart. J. Roy. Meteor. Soc.*, **122**, 669–688.

Moncrieff, M. W., M. A. Shapiro, J. M. Slingo, and F. Molteni, 2007: Collaborative research at the intersection of weather and climate. *WMO Bulletin*, **56 (3)**, 204–211.

Moncrieff, M. W., D. E. Waliser, M. J. Miller, M. a. Shapiro, G. R. Asrar, and J. Caughey, 2012: Multiscale convective organization and the YOTC virtual global field campaign. *Bull. Amer. Meteor. Soc.*, **93 (8)**, 1171–1187, doi:10.1175/BAMS-D-11-00233.1.

Nakazawa, T., 1988: Tropical super clusters within intraseasonal variations over the western pacific. *J. Meteor. Soc. Japan.*, **66**, 823–839.

Salby, M. L. and H. H. Hendon, 1994: Intraseasonal behavior of clouds, temperature, and motion in the Tropics. *J. Atmos. Sci.*, **51 (15)**, 2207–2224.

Sauer, T., J. A. Yorke, and M. Casdagli, 1991: Embedology. *J. Stat. Phys.*, **65 (3–4)**, 579–616, doi:10.1007/bf01053745.

Shinoda, T., H. H. Hendon, and J. Glick, 1998: Intraseasonal variability of surface fluxes and sea surface temperature in the tropical western Pacific and Indian Oceans. *J. Climate*, **11 (1995)**, 1685–1702.

Sui, C. and K. Lau, 1992: Multiscale Phenomena in the Tropical Atmosphere over the Western Pacific. *Mon. Wea. Rev.*, **120**, 407–430.

Sui, C.-H., K.-M. Lau, Y. N. Takayabu, and D. a. Short, 1997: Diurnal Variations in Tropical Oceanic Cumulus Convection during TOGA COARE. *J. Atmos. Sci.*, **54 (5)**, 639–655, doi:10.1175/1520-0469(1997)054⟨0639:DVITOC⟩2.0.CO;2.

Takayabu, Y. N., 1994: Large-scale cloud disturbances associated with equatorial waves. Part I: Spectral features of the cloud disturbances. *Journal of the Meteorological Society of Japan*, **72 (3)**, 433–449.

Tian, B., D. E. Waliser, and E. J. Fetzer, 2006: Modulation of the diurnal cycle of tropical deep convective clouds by the MJO. *Geophysical Research Letters*, **33 (20)**, 1–6, doi:10.1029/2006GL027752.

Tung, W.-w., J. Gao, J. Hu, and L. Yang, 2011: Detecting chaos in heavy-noise environments. *Phys. Rev. E*, **83 (4)**, 1–9, doi:10.1103/PhysRevE.83.046210.

Tung, W.-w., D. Giannakis, and A. J. Majda, 2013: Symmetric and antisymmetric signals in MJO deep convection. Part II: Kinematics and thermodynamics associate with equatorial and off-equatorial convection. *J. Atmos. Sci., to be submitted*.

Tung, W.-w., C. Lin, B. Chen, M. Yanai, and A. Arakawa, 1999: Basic modes of cumulus heating and drying observed during TOGA-COARE IOP. *Geophys. Res. Lett.*, **26 (20)**, 3117–3120.

Waliser, D., 2005: Predictability and forecasting. *Intraseasonal Variability in the Atmosphere-Ocean Climate System*, W. K. Lau and D. E. Waliser, Eds., Springer, 389–423.

Waliser, D. E., et al., 2009: MJO simulation diagnostics. *J. Climate*, **22 (11)**, 3006–3030, doi:10.1175/2008JCLI2731.1.

Wang, B. and F. Liu, 2011: A model for scale interaction in the Madden-Julian oscillation. *J. Atmos. Sci.*, **68 (11)**, 2524–2536, doi:10.1175/2011JAS3660.1.

Wang, B. and H. Rui, 1990: Synoptic climatology of transient tropical intraseasonal convection anomalies: 1975-1985. *Meteor. Atmos. Phys.*, **44**, 43–61.

Webster, P. and R. Lukas, 1992: TOGA COARE: The Coupled Ocean-Atmosphere Response Experiment. *Bull. Amer. Meteor. Soc.*, **73 (9)**, 1377–1416.

Wheeler, M. and G. N. Kiladis, 1999: Convectively coupled equatorial waves: Analysis of clouds and temperature in the wavenumber-frequency domain. *J. Atmos. Sci.*, **56 (3)**, 374–399, doi:10.1175/1520-0469(1999)056⟨0374:CCEWAO⟩2.0.CO;2.

Wheeler, M. C. and H. H. Hendon, 2004: An all-season real-time multivariate MJO index: Development of an index for monitoring and prediction. *Mon. Wea. Rev.*, **132 (8)**, 1917–1932, doi:10.1175/1520-0493(2004)132⟨1917:AARMMI⟩2.0.CO;2.

Yanai, M., B. Chen, and W.-w. Tung, 2000: The Madden-Julian oscillation observed during the TOGA COARE IOP: Global view. *J. Atmos. Sci.*, **57 (15)**, 2374–2396, doi:10.1175/1520-0469(2000)057⟨2374:TMJOOD⟩2.0.CO;2.

Yanai, M. and M. Murakami, 1970: Spectrum analysis of symmetric and antisymmetric equatorial waves. *J. Meteor. Soc. Japan*, **48 (4)**, 331–347.

Yasunari, T., 1979: Cloudiness Fluctuations Associated with the Northern Hemisphere Summer Monsoon. *J. Meteor. Soc.Japan*, **57 (3)**, 227–242.

Zhang, C. and M. Dong, 2004: Seasonality in the Madden-Julian oscillation. *J. Climate*, **17**, 3169–3180.

# List of Figures

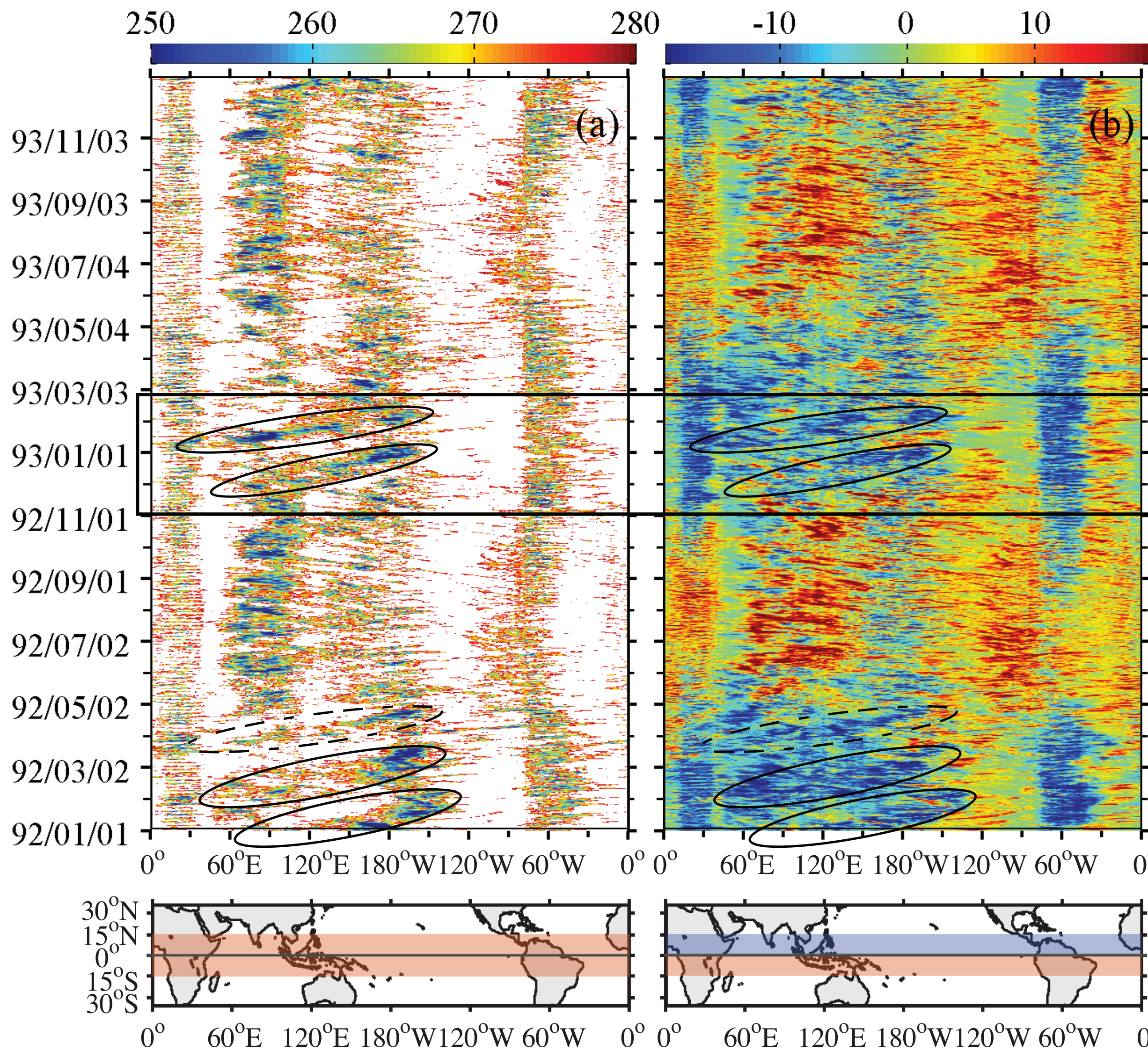


FIG. 1. Time-longitude section of (a) symmetric and (b) antisymmetric brightness temperature $T_B$ data (in K) from CLAUS for the period 1992–1993. In (a) only thresholded values $< 280$ K are shown to emphasize convective activity. The bottom map in (a) indicates that the symmetric component was obtained via averaging over 15°S to 15°N. The antisymmetric component in (b) was obtained by subtracting the values at the northern latitudes from the corresponding southern latitudes. The boxed interval corresponds to the TOGA-CORE IOP. Ovals mark significant MJO events.

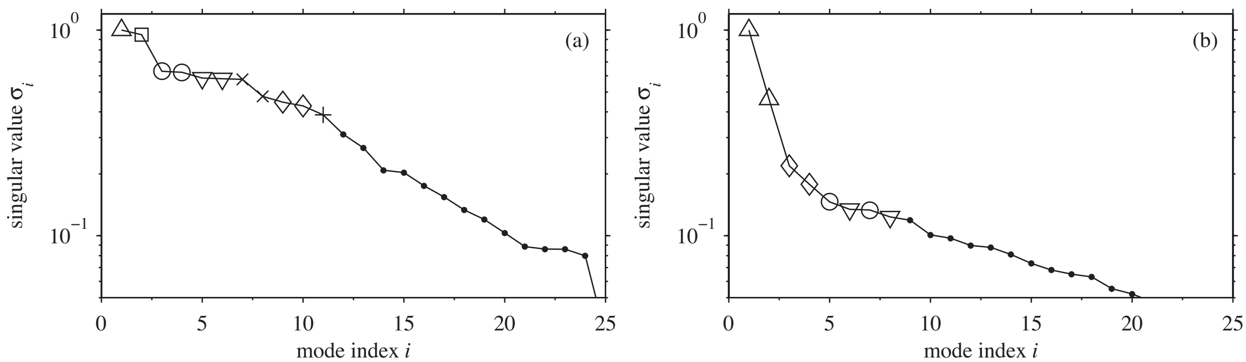


FIG. 2. Singular values $\sigma_i$ of the NLSA modes for (a) the symmetric, and (b) antisymmetric data. (Triangles) Annual; (Square) interannual; (Diamonds) semiannual; (Circles) MJO; (Upturned triangles) diurnal; ($\times$) Indo-Pacific intraseasonal–interannual; (+) Maritime Continent modes.

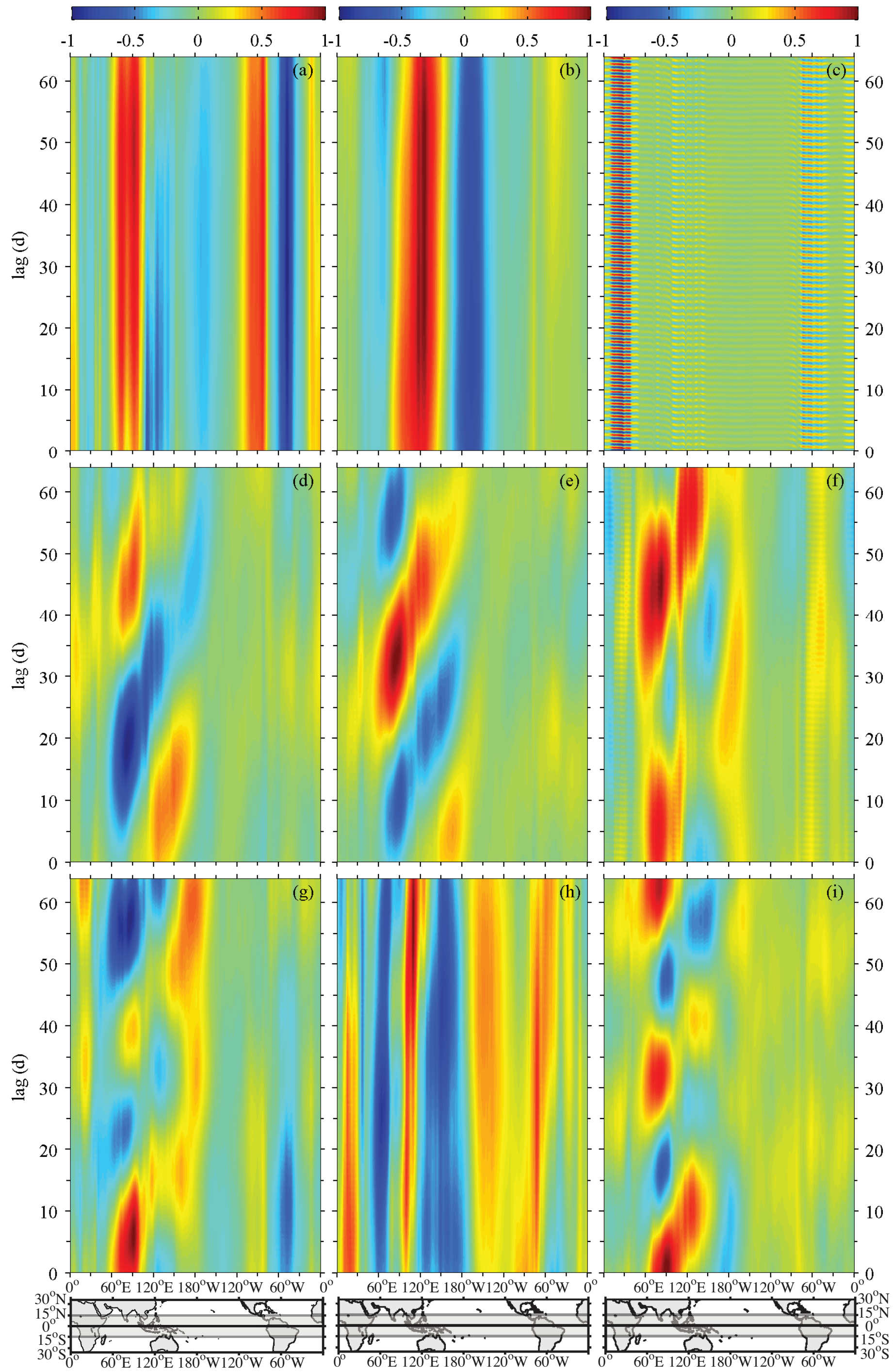


FIG. 3. Left singular vectors $\mathbf{u}_i$ (spatiotemporal patterns) for the symmetric NLSA modes highlighted in Fig. 2. (a) Annual mode, $\mathbf{u}_1$; (b) interannual mode, $\mathbf{u}_2$; (c) first diurnal mode, $\mathbf{u}_5$ (Diurnal1); (d,e) MJO pair, $\mathbf{u}_3$ and $\mathbf{u}_4$ (MJO1, MJO2); (f,g) intraseasonal–interannual modes, $\mathbf{u}_7$ and $\mathbf{u}_8$; (h) first intraseasonal–semiannual mode, $\mathbf{u}_9$; (i) Maritime Continent mode, $\mathbf{u}_{11}$. Modes $\mathbf{u}_6$ and $\mathbf{u}_{10}$ are qualitatively similar to modes $\mathbf{u}_5$ and $\mathbf{u}_9$, respectively, and therefore not shown here for brevity. The vertical axes measure time within the $\Delta t = 64$ d embedding window.

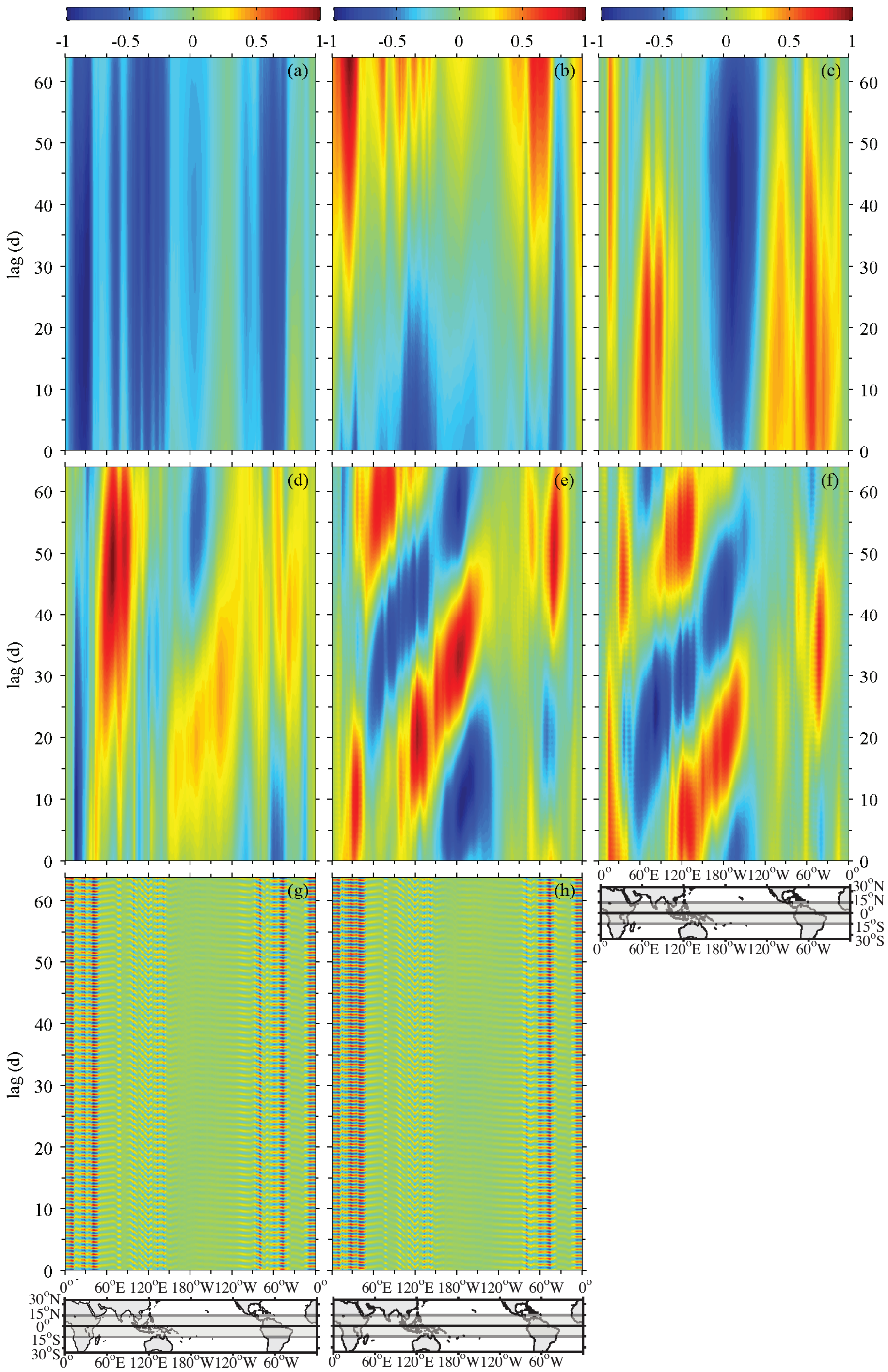


FIG. 4. Left singular vectors $\mathbf{u}_i$ (spatiotemporal patterns) for the antisymmetric NLSA modes highlighted in Fig. 2. (a,b) Annual modes, $\mathbf{u}_1$ and $\mathbf{u}_2$; (c) semiannual–interannual mode, $\mathbf{u}_3$; (d) intraseasonal–semiannual mode, $\mathbf{u}_4$; (e,f) MJO pair, $\mathbf{u}_5$ and $\mathbf{u}_7$ (MJO1$_\mathrm{A}$, MJO2$_\mathrm{A}$); (g,h) diurnal pair (Diurnal1$_\mathrm{A}$, Diurnal2$_\mathrm{A}$) $\mathbf{u}_6$ and $\mathbf{u}_8$. The vertical axes measure time within the $\Delta t = 64$ d embedding window.

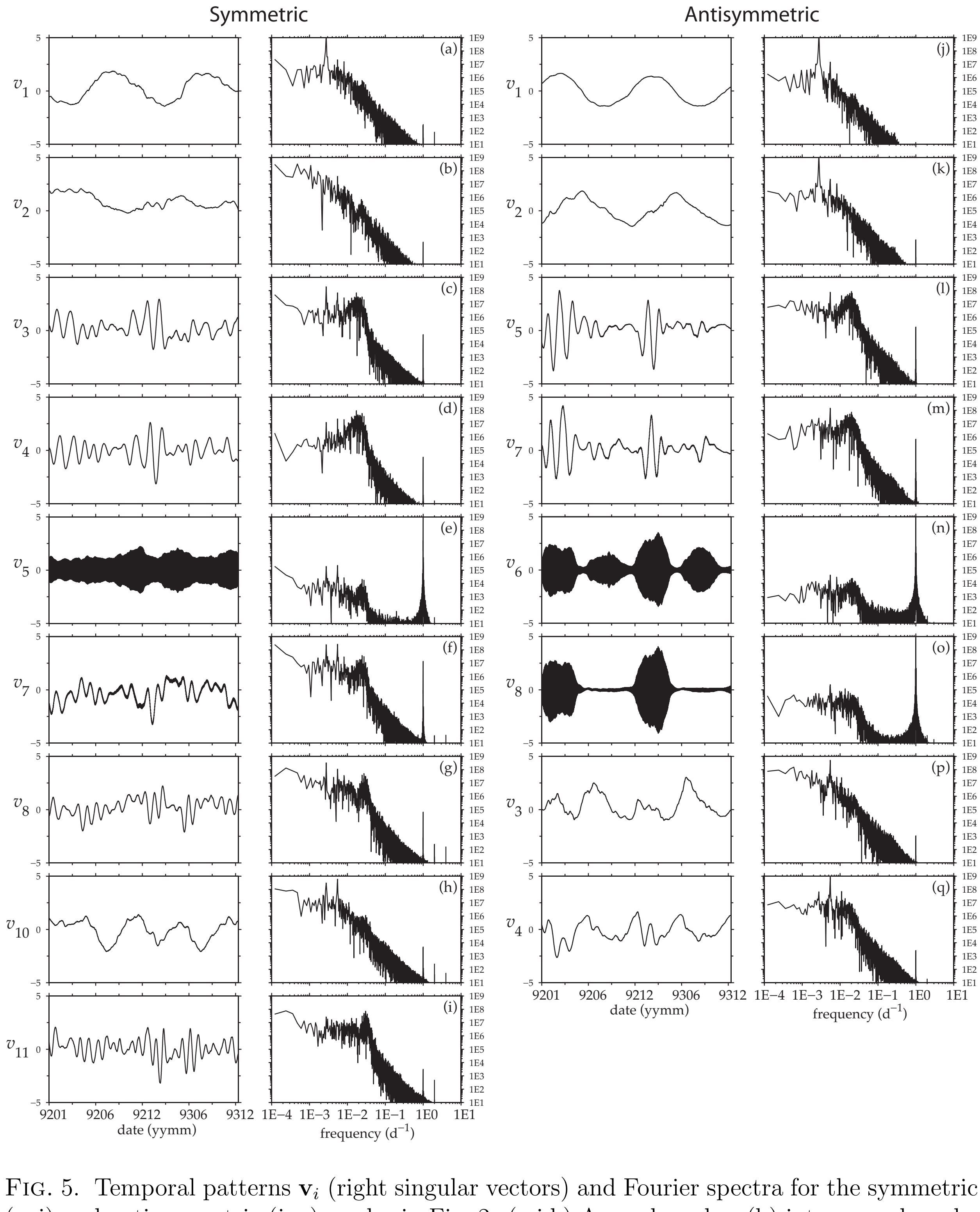


FIG. 5. Temporal patterns $\mathbf{v}_i$ (right singular vectors) and Fourier spectra for the symmetric (a–i) and antisymmetric (j–q) modes in Fig. 2. (a,j,k) Annual modes; (b) interannual mode; (c,d and l,m) MJO pairs; (e) first symmetric diurnal mode; (f,g) Indo-Pacific intraseasonal–interannual modes; (h,p,q) semiannual modes; (i) Maritime Continent mode; (m,n) antisymmetric diurnal pair. The temporal patterns of symmetric modes $v_6$ and $v_{10}$ are qualitatively similar to modes $v_5$ and $v_9$, respectively, and therefore not shown for conciseness.

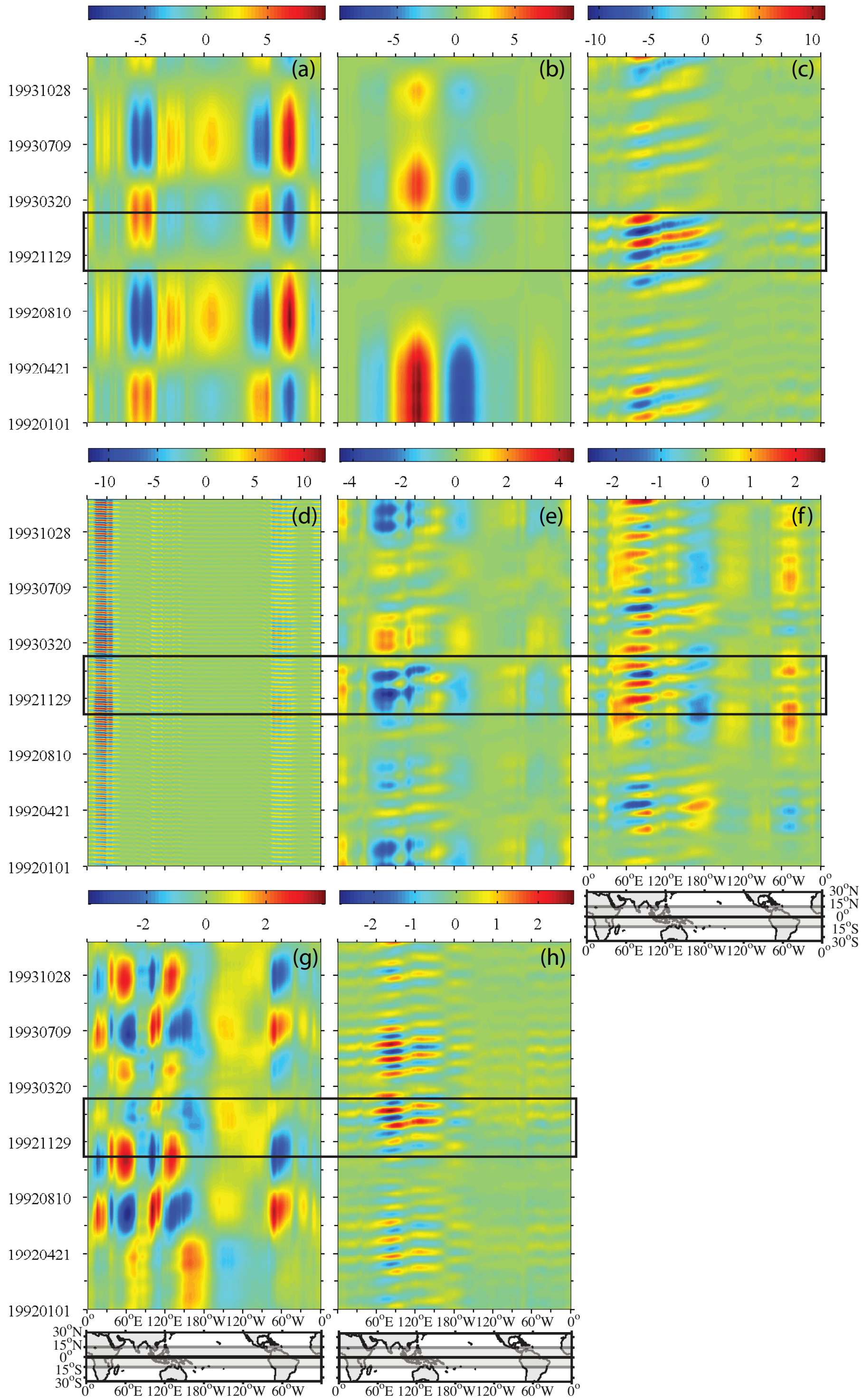

FIG. 6. Spatiotemporal reconstructions of the symmetrically averaged $T_B$ field ($\overline{T_B(\Lambda, t)}$, in K) for 1992–1993 using NLSA. (a) Annual mode ($i = 1$); (b) interannual mode ($i = 2$); (c) symmetric MJO pair ($i = 3, 4$); (d) symmetric diurnal pair ($i = 5, 6$); (e,f) Indo-Pacific intraseasonal–interannual modes ($i = 7$ and $i = 8$); (g) semiannual pair ($i = 9, 10$); (h) Maritime Continent mode ($i = 11$). The boxed interval corresponds to the TOGA-CORE IOP.

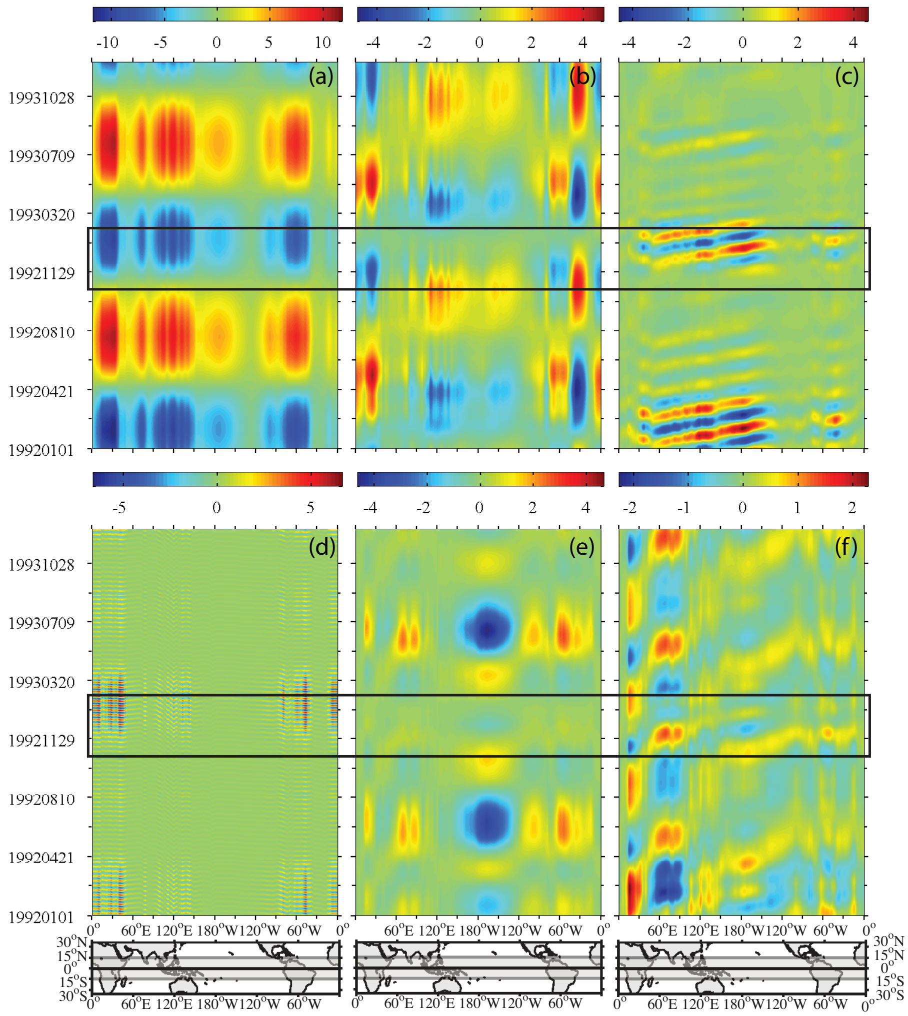


FIG. 7. Similar to Fig.6, but for spatiotemporal reconstructions of the antisymmetrically averaged $T_B$ field ($\overline{T_B(\Lambda, t)}_A$, in K) for 1992–1993 using NLSA. (a,b) annual modes ($i = 1$ and $i = 2$); (c) antisymmetric MJO pair ($i = 5, 7$); (d) antisymmetric diurnal pair ($i = 6, 8$); (e) semiannual–interannual mode, $i = 3$; (f) intraseasonal–semiannual mode, $i = 4$.

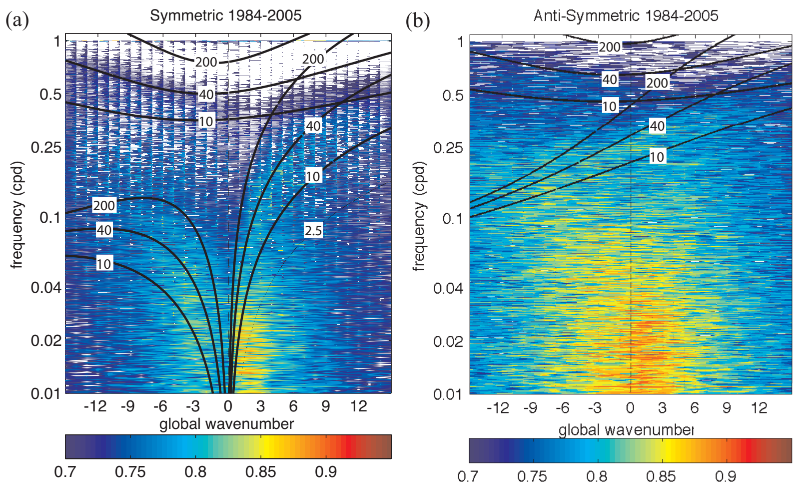


FIG. 8. Raw frequency-wavenumber power spectra for (a) symmetric and (b) antisymmetric CLAUS $T_B$ data ($\overline{T_B(\Lambda,t)}$ and $\overline{T_B(\Lambda,t)}_A$, in K) for the period 1984–2005. Logarithms of powers normalized by the domain maximum with resulting values $\geq 0.7$ are shown. The ordinates are scaled logarithmically. The dispersion curves shown are (a) meridional mode, $n = 1$ inertio-gravity waves and equatorial Rossby waves, and equatorial Kelvin waves; (b) meridional mode, $n = 0$ eastward-propagating inertio-gravity waves and mixed Rossby-gravity waves, and $n = 2$ inertio-gravity waves.The associated equivalent depths are in m.

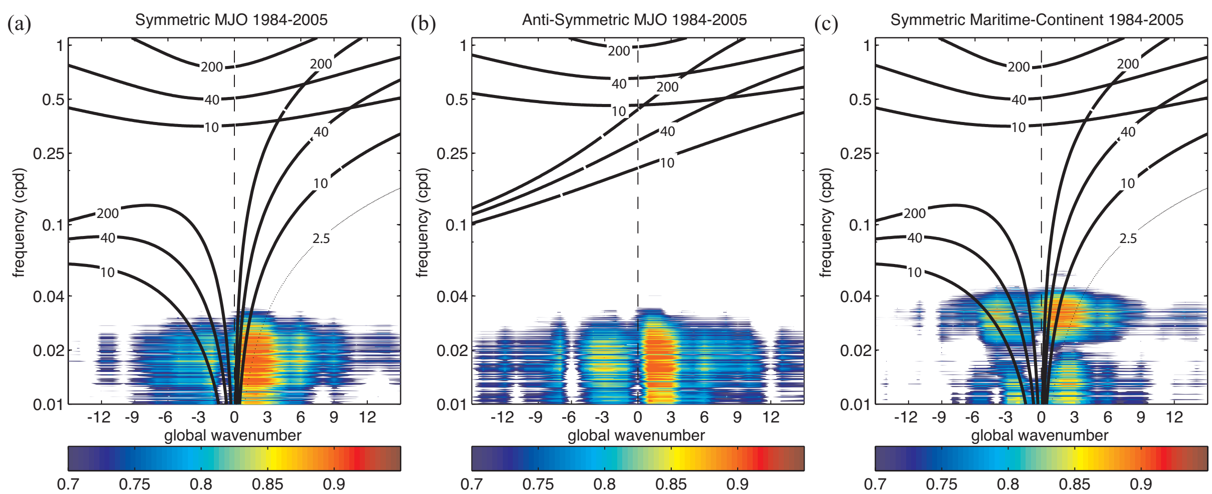


Fig. 9. Same as Fig. 8, but for (a) symmetric MJO; (b) antisymmetric MJO; (c) symmetric Maritime Continent modes.

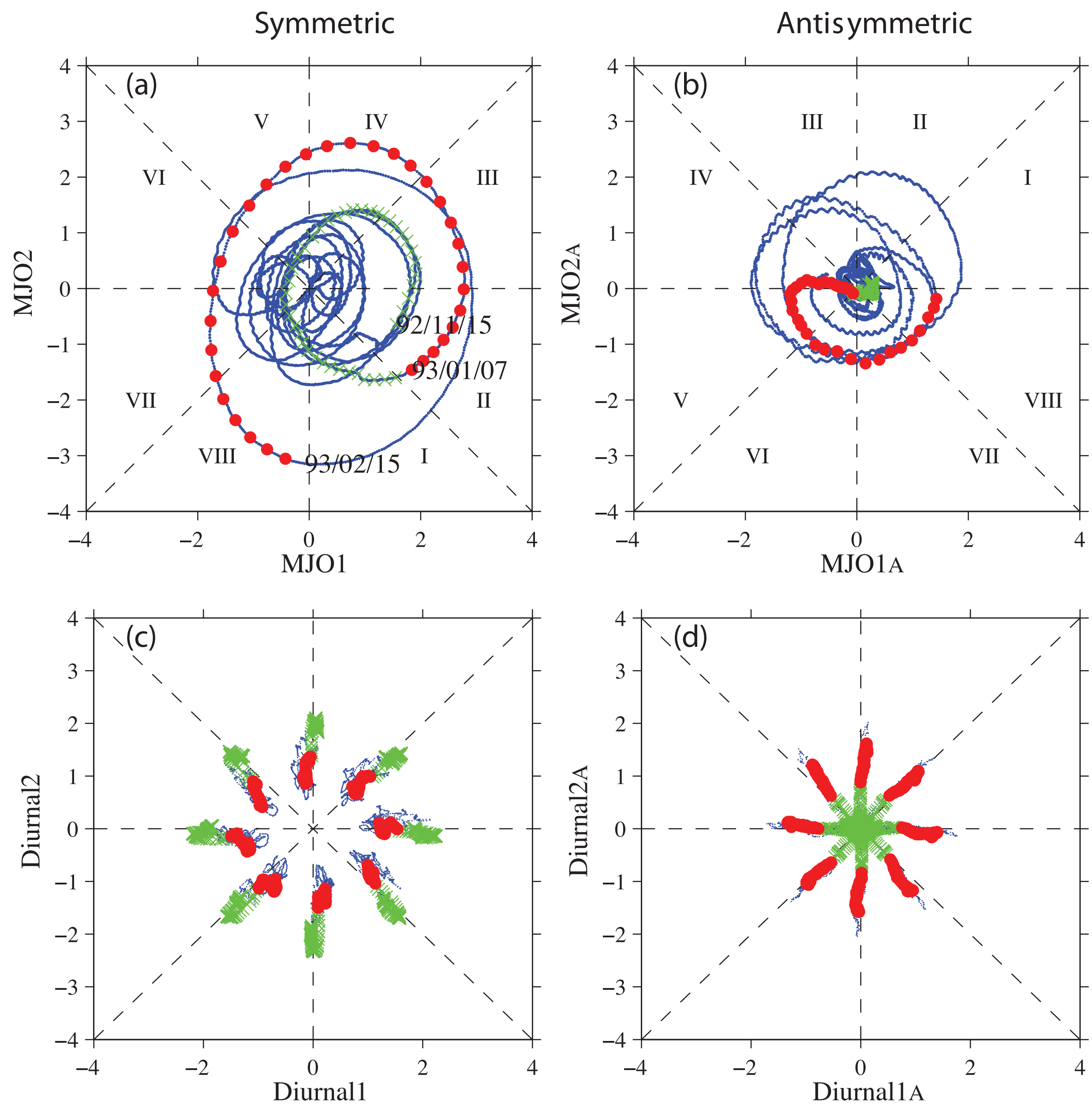


FIG. 10. Phase space diagrams for 1992–1993. (a) Symmetric MJO pair (MJO1, MJO2); (b) antisymmetric MJO pair ($MJO1_A$ and $MJO2_A$); (c) symmetric diurnal pair (Diurnal1 and Diurnal2); (d) antisymmetric diurnal pair ($Diurnal1_A$ and $Diurnal2_A$). The green crosses (X) mark the weaker MJO event observed during TOGA-COARE IOP from mid-November 1992 to early January 1993. The red dots (O) mark the later, stronger event terminating in mid-February 1993. Roman numerics in (a) and (b) denote the eight MJO phases, calibrated against the COARE IOP events so that they correspond to a sequence of enhanced eastward-propagating convective activity from the Eastern to Western Hemispheres.

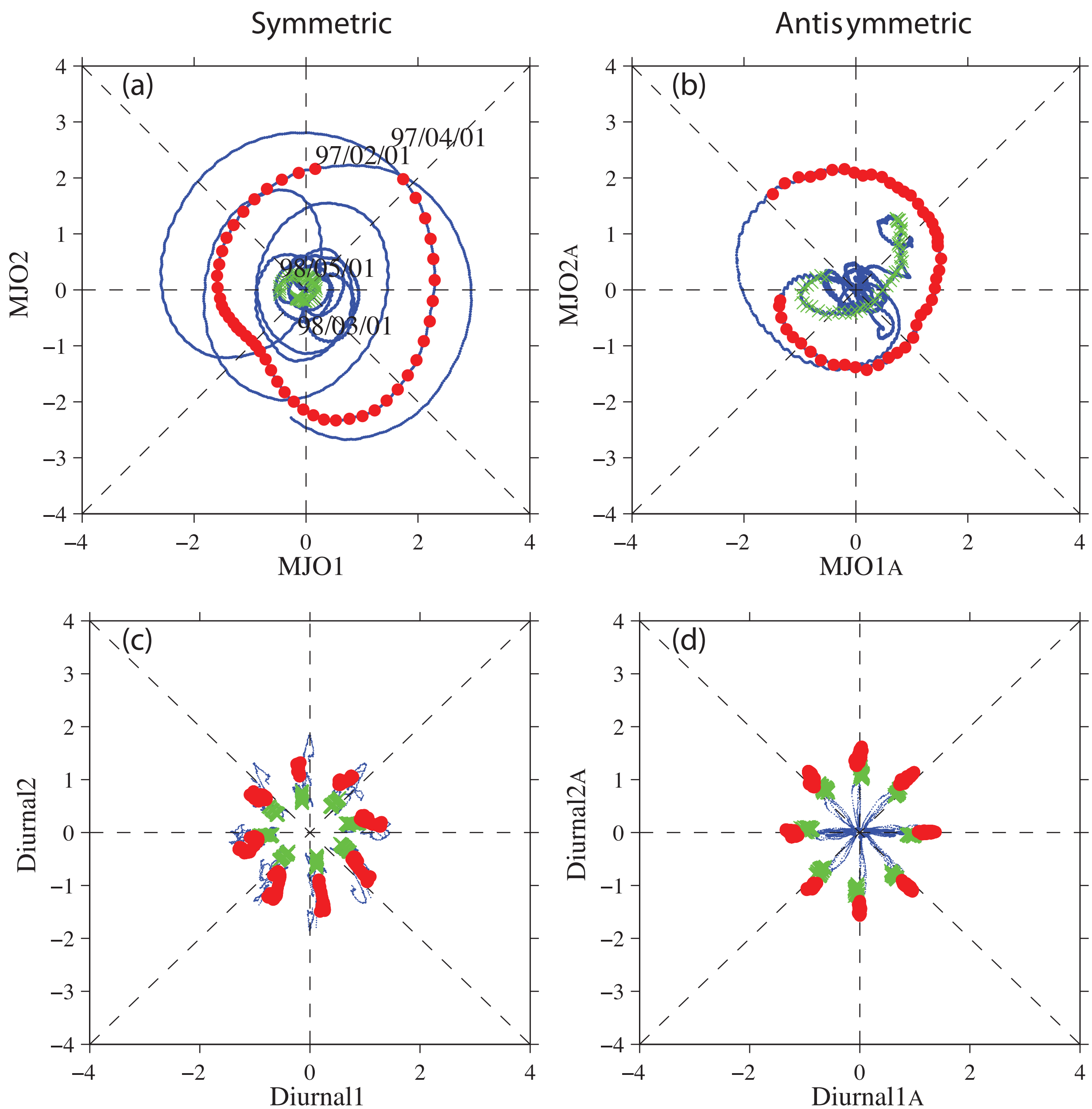


FIG. 11. Similar to Fig. 10, except for phase space diagrams for 1997–1998.The red dots (O) mark the strong MJO event occurring from February to April 1997 during ENSO amplification. The green crosses (X) mark the weak MJO occurring from March to May 1998 during strong ENSO.

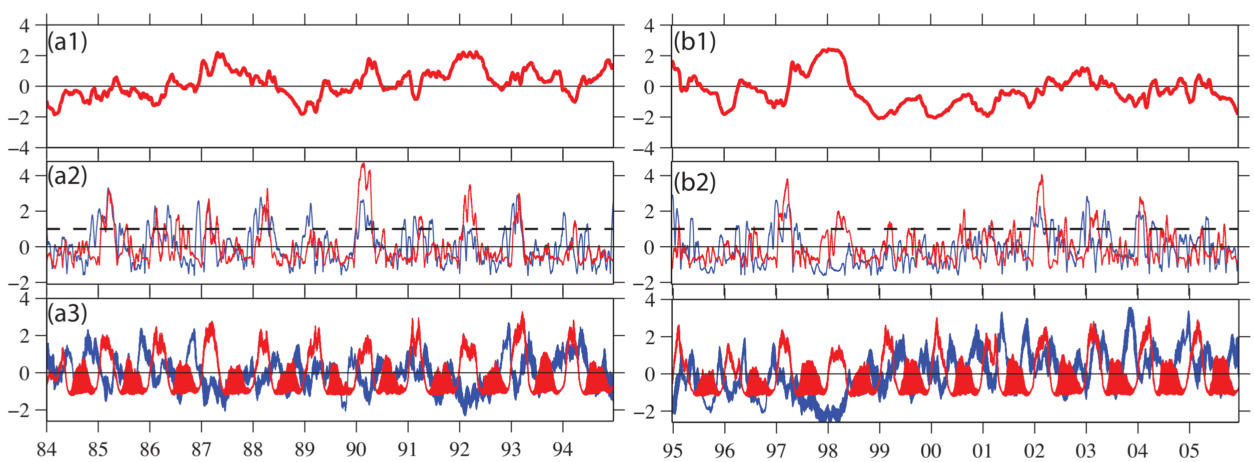


FIG. 12. Temporal patterns for (a) 1984–1994 and (b) 1995-2005. (a1, b1) Symmetric interannual mode (red) normalized by its standard deviation; (a2,b2) standardized magnitudes of the symmetric (blue) and antisymmetric (red) MJO modes, with dashed lines marking one standard deviation above the mean (i.e., zero in the standardized series); (a3, b3) standardized magnitudes of the symmetric (blue) and antisymmetric (red) diurnal modes.

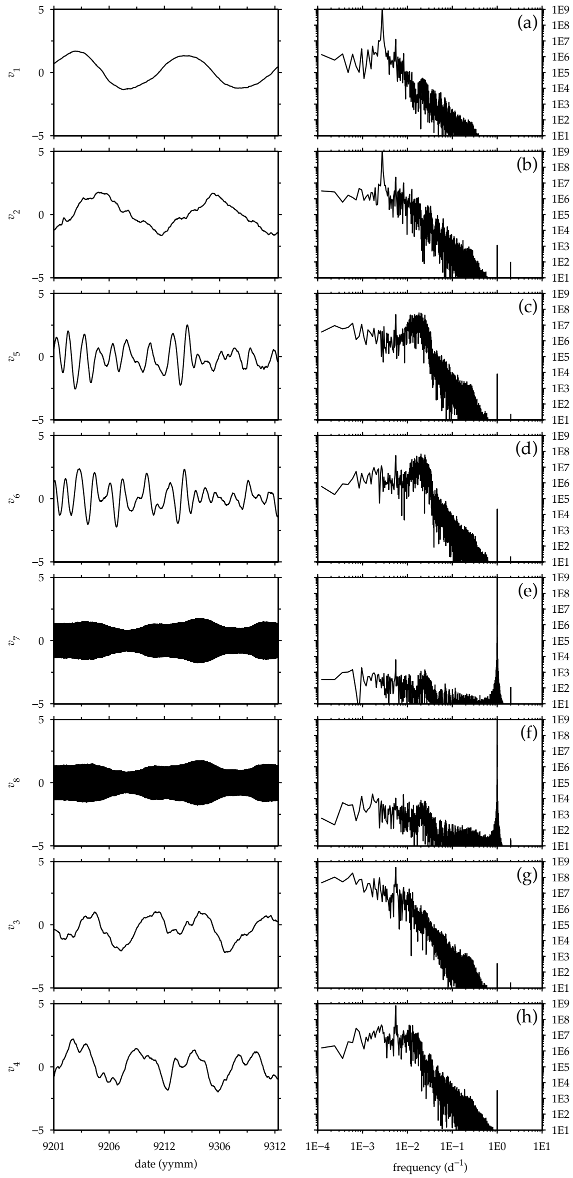


FIG. 13. Temporal patterns $\mathbf{v}_i$ (right singular vectors) and Fourier spectra for the anti-symmetric modes from SSA. (a,b) Annual modes; (c,d) MJO pair; (e,f) diurnal pair; (g,h) semiannual modes.

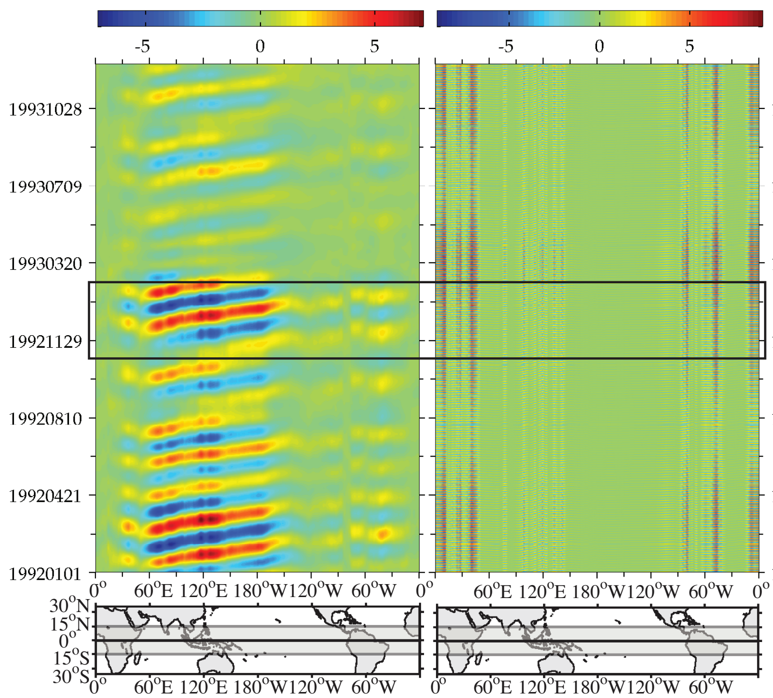


Fig. 14. Spatiotemporal reconstructions of the antisymmetrically averaged $T_B$ field (in K) for 1992–1993 using SSA. (a) MJO pair; (b) diurnal pair. The boxed interval corresponds to the TOGA-CORE IOP.